NUMERICAL MODELING OF CIRCULATORS

Circulators are a key control component of microwave and millimeter-wave electronic systems. They are found in commercial and military equipment, including receiving, transmitting, and dual-purpose systems. Circulators are used in ship, satellite, aircraft and land-based equipment. Because all of this equipment has been under ever increasing pressure to become lighter, smaller, and more reliable over the last three decades, coinciding with the semiconductor and integrated circuit revolutions in technology, microwave and millimeter-wave components have converted from hollow or partly filled waveguiding structures to those compatible with planar configuration.

Planar configuration enables the circuit designer to use either hybrid or integrated circuit technology. Hybrid technology is more flexible in that it allows the designer to combine components prepared with different procedures, and then joined in a planar format for final assembly. Thus the solid-state field effect transistors (FETs) would be attached to a substrate that already had microstrip lines etched for the creation of transmission lines (single or coupled). Devices such as circulators also would be glued on with external biasing magnet circuits after the preparation of the substrate. This process would continue until the entire system was completed, and then the assembled structure dropped into a housing with the proper connectors piercing the housing at designated sites.

Although hybrid circuits were prepared for over two decades in industrial facilities, they have several serious drawbacks. One is the effort required to assemble such circuits. The cost in time and labor can be high. Another is the fact that circuits prepared in the hybrid format are all different. No two completed circuits look or act electrically alike. Thus, to keep finished circuits within performance specifications, careful technician tuning of each circuit coming off the assembly line had to be done. Such tuning can be extremely labor-intensive, and no amount of it can save some circuits. Finally, circuits that have made it through the first two stages, fabrication and tuning, may fail in actual use. This is because hybrid circuits are composed of many weak bonds, whether between a wire and a metallization on the substrate or between two planar substrates in a housing having many of them.

To eliminate the many problems associated with hybrid circuit technology, an increasingly aggressive move toward monolithic integrated circuits (MICs) began in the late 1970s, accelerated in the 1980s, and became mature in the 1990s. The basic idea behind this newer technology was to utilize the advantages the semiconductor manufacturers had obtained in producing hundreds of thousands of miniature solid-state active and passive components of exactly the same properties. They did it by using step-and-repeat fabrication techniques on single crystal silicon and gallium arsenide wafers of precise thickness and uniform properties. The uniformity of the semiconductor wafers was assured by growing single crystal boules of the desired elemental or compound semiconductors. Devices were fabricated by ion implanting, diffusing, or depositing in or on the wafer the selected atoms, using vacuum chambers or furnaces.

There was no reason, in principle, why MIC methods could not be adapted for microwaves and millimeter waves, and once the idea caught on, there was no turning back. Microwave monolithic integrated circuits (MMICs) became the next technology revolution.

Fabrication of circulators in the hybrid format began in the 1960s and 1970s, and included such structures as ferrite devices prepared by dropping a ferrite puck into a hole machined into a substrate material, metallizing the shield and microstrip lines, and then placing the whole assembly in a housing. This concept extended itself in the 1980s and 1990s into having the circulator device prepared on the same substrate as other microwave and millimeter-wave components. The latter approach is almost monolithic, except for the separate machining phase and separate ferrite puck processing steps.

Then came the idea in the 1990s of developing both advanced hybrid circulator assembly and monolithic circulator processing. Formation of the DARPA (Defense Advanced Research Project Agency) Ferrite Development Consortium (FDC), a group of industrial, government, and university research laboratories, led to progress in preparing monolithically compatible circulators on silicon and gallium arsenide substrates. This research effort happened between 1993 and 1996, with spinoffs occurring several years after the completion of the FDC's work.

Essential to the capability to design hybrid and monolithic circulators is the ability to model the performance of the nonreciprocal component so that it will not have to be redesigned many times at tremendous expense. A major breakthrough in the effort to provide a design-friendly tool was the development of a two-dimensional (2-D) uniform Green's function method by Bosma (1) in the early 1960s. The method worked well because its Green's function expression for the electric field normal to the shield depends on an expansion whose terms are convergent. Because it is based upon a canonical circular geometry, and the main physical purpose of the Green's function is to take proper account of the nonreciprocating anisotropy of the ferrite material under appropriate boundary conditions, the expression can be evaluated very rapidly.

Other electromagnetic techniques were examined from the 1960s onward for planar circulators, and all of these methods, including the boundary-element method, the finite-element method, and the finite-difference method, are amenable to analyzing devices with arbitrary or nonstandard perimeters, but are extremely numerically intensive. They have their place in the suite of techniques employed to realize a final device, but for user-friendly device design, where rapid repetitive trials are performed to find a final acceptable design with the proper characteristics, it is most desirable to use a Green's function method. Though the Green's function technique works only for a circular shape and some other simple canonical geometries, it can be used to good approximation for other, nonstandard shapes to obtain the basic design information required before switching to the use of the costly and slow numerically intensive solvers. Also, because the circular shape is very popular, oftentimes the use of the Green's function method will provide the exact solution for design.

COMPUTER-AIDED DESIGN OF PLANAR CIRCULATORS

Computer-aided design of ferrite circulators is made easy with the use of Green's-function-based computer codes. Since the thickness of the substrate is a fraction of a wavelength, the higher-order perpendicular mode structure is limited, as is the launching of surface waves. The lack of surface waves is desirable for maintaining a controllable mode structure inside the circulator, as well as in the input and output transmission lines, which can be microstrip or coplanar. The thin substrate also means that a 2-D representation of the electromagnetic fields within the circulator device is a reasonable approximation. The device may be modeled be letting waves enter and exit through specific ports, and assuming that no energy escapes through the intervening perimeter contour regions between ports. This means that magnetic walls are assumed at interfaces between the ferrite and the external dielectric. Such condition forms are what is referred to as the hard wall condition. For such a condition, Green's functions are available for both a homogeneous and an inhomogeneous 2-D ferrite puck.

The inhomogeneous case is very important, since the situation of nonuniformly applied magnetic bias field, finite-sized puck, and nonuniform ferrite material distribution throughout the puck radius all lead to violation of the uniformity assumption. So although the uniform Green's function may be a decent first approximation on the way to getting a circulator design, it can actually be only a rough estimate or even a bad approximation if the magnetic bias nonuniformities become large or if intentional variation of the ferrite material magnetization $\boldsymbol{M}$ is significant. For almost all cases then it is recognized that inhomogeneous Green's functions are required. Thus the uniform 2-D Green's function must be replaced in many circumstances by an inhomogeneous 2-D Green's function.

Whether the problem being addressed is uniform or nonuniform, the designer may be left with the need to assess the effect of the external dielectric medium. This can be done using a specially prepared Green's function that allows some leakage of the electromagnetic wave into the surrounding dielectric region, while maintaining the basic electromagnetic function of the device, which is to exchange energy between the multiport device terminals.

Green's functions that can represent circulator behavior for an arbitrary number of ports, with arbitrary angular locations along the device perimeter, exist even at present. But great economy of computational effort results if the distribution of the ports along the perimeter is manyfold symmetric. This is assured if the ports are chosen to be of equal angular width and placed regularly along the circumference of the device. Once this is done, the perimeter Green's functions, relating a source at one point along the perimeter to a resulting field at another point along the perimeter, have symmetry relations to one another, vastly reducing the computer times for running simulations of the circulator.

All the above arguments relating to the nature of the puck (uniform versus inhomogeneous), the wall characteristic (hard wall versus soft wall), and the properties of ports (arbitrary versus symmetric disposition) apply equally well for two- and three-dimensional circulator models. As already mentioned, the 2-D model approach is quite reasonable for many if not most experimentally encountered situations. However, where specific study of the substrate thickness effect of the circulator performance is desired, the designer must resort to using rigorously derived three-dimensional (3-D) Green's functions.

To find the complete electromagnetic field, dyadic Green's function solutions must be sought and satisfactory forms obtained that will enable convenient representations for numerical evaluation. This is because for the 2-D models, the electric field component (E_z) and the magnetic field components (H_x, H_y or H_r, H_ϕ in cylindrical coordinates) must be determined by the driving function (or source). The source may be a current vector (or its equivalent components), an electric field vector, or a magnetic field vector on a contour or surface. The source location exciting the circulator device is on a contour if the model is 2-D, and on a surface if the model is 3-D. For the 3-D model the dyadic Green's function is much more complicated because the electric and magnetic field vectors are full (E_x, E_y, E_z and H_x, H_y, H_z must be considered; equivalently, E_r, E_ϕ, E_z and H_r, H_ϕ, H_z in cylindrical coordinates).

FERRITE MATERIAL PARAMETERS AFFECTING MODELING

Nonreciprocity is generated in the circulator device (Fig. 1) by applying a bias dc magnetic field perpendicular to the planar surface of the structure, be it hybrid or monolithic. The bias field will create off-diagonal tensor elements in the permeability, and these new elements are antisymmetrically disposed with respect to the diagonal. The size of the off-diagonal element κ compared with the diagonal element μ will determine the extent of nonreciprocal action possible in a circulator device. The permeability tensor is

$$\overleftrightarrow{\mu} = \mu_0 \begin{bmatrix} \mu & -j\kappa & 0 \\ j\kappa & \mu & 0 \\ 0 & 0 & 1 \end{bmatrix} \tag{1}$$

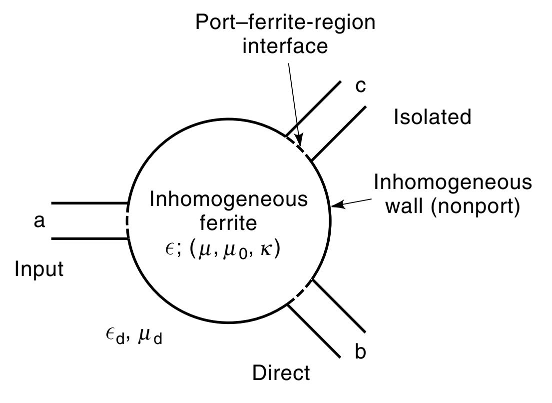

Figure 1. Top view of a microstrip circulator, valid for either a 2-D or a 3-D representation. In the 3-D case it represents a cross-section cut at z = const through the device. The drawing is done for the case of symmetrically disposed ports (three here). Under the central shield is the ferrite material. Microstrip lines provide access to the external environment. The inhomogeneous wall between ports is either a magnetic wall or a ferrite–dielectric interface.

where μ_0 is the free-space value. μ and κ (relative values) have both real and imaginary parts when the system is lossy, as is any real ferrite material. Thus, in phasor form (assuming an $e^{j\omega t}$ time dependence) we have by Soohoo (2)

$$\mu = \mu' - j\mu'' \tag{2}$$

$$\kappa = \kappa' - j\kappa'' \tag{3}$$

$$\mu' = 1 + \frac{\omega_m\omega_0[\omega_0^2 - \omega^2(1-\alpha_m^2)]}{[\omega_0^2 - \omega^2(1+\alpha_m^2)]^2 + 4\omega^2\omega_0^2\alpha_m^2} \tag{4a}$$

$$\mu'' = \frac{\omega_m\omega\alpha_m[\omega_0^2 + \omega^2(1+\alpha_m^2)]}{[\omega_0^2 - \omega^2(1+\alpha_m^2)]^2 + 4\omega^2\omega_0^2\alpha_m^2} \tag{4b}$$

$$\kappa' = -\frac{\omega_m\omega[\omega_0^2 - \omega^2(1+\alpha_m^2)]}{[\omega_0^2 - \omega^2(1+\alpha_m^2)]^2 + 4\omega^2\omega_0^2\alpha_m^2} \tag{5a}$$

$$\kappa'' = -2\frac{\omega_0\omega^2\alpha_m\omega_m}{[\omega_0^2 - \omega^2(1+\alpha_m^2)]^2 + 4\omega^2\omega_0^2\alpha_m^2} \tag{5b}$$

Controlling variables in these equations are the magnetization radian frequency ω_m, ferromagnetic resonance radian frequency ω_0, phenomenological damping term α_m, and operating radian frequency ω. The first three frequencies can be found by

$$\omega_m = -\gamma M \tag{6}$$

$$\omega_0 = -\gamma H_i \tag{7}$$

$$\alpha_m = -\frac{\gamma\,\Delta H}{2\omega} \tag{8}$$

Here γ is the gyromagnetic ratio, whose value in rationalized MKS units is -2.21265×10^5 (rad/s)/(A/m) $= 2\pi \times 2.8$ MHz/Oe. M is the magnetization, which may approach a saturated value M_s; ΔH the ferromagnetic linewidth; and H_i the internal magnetic field, which may be expressed as a superposition of the net internal field due to externally applied field H_{ap} and the anisotropy field H_{an}:

$$H_i = H_{i(ap)} + H_{an} \tag{9}$$

The internal magnetic bias field $H_{i(ap)}$ has previously been approximated using a demagnetization factor N_{zz} (for the preferred direction z):

$$H_{i(ap)} = H_{ap} - 4\pi N_{zz} M \tag{10}$$

M is assumed to be in the z direction also. When saturation has been attained, M is replaced by M_s. Of course, the resultant field is not necessarily only in the z direction even if the applied field is. Equation (10) represents then an approximation of further implications, other than its scalar form. In vector form, we have

$$\boldsymbol{H}_{i(ap)} = \boldsymbol{H}_{ap} - 4\pi \boldsymbol{N}\cdot\boldsymbol{M} \tag{11}$$

The demagnetization factor N_{zz}, which is a function of the radial location r within the circulator puck R ($r \le R$), has the property

$$N_{zz} = N_{zz}(r,z) \le 1 \tag{12}$$

The last term in Eqs. (10) and (11) is referred to as the demagnetization field, allowing us to rewrite these two equations as

$$H_{i(ap)} = H_{ap} - H_{de} \tag{13a}$$

$$H_{de} = 4\pi N_{zz} M \tag{13b}$$

$$\boldsymbol{H}_{i(ap)} = \boldsymbol{H}_{ap} - \boldsymbol{H}_{de} \tag{14a}$$

$$\boldsymbol{H}_{de} = 4\pi \boldsymbol{N}\cdot\boldsymbol{M} \tag{14b}$$

If it is desired to avoid the approximation implied by the designations in Eqs. (13b) and (14b), then the problem must be solved fully by numerical means, self-consistently obtaining the static field solution inside and outside the ferrite puck, whatever its geometric shape. This holds true whether the shape is a thin cylindrical volume, or a more irregular shape such as a hexagonal prism.

For finite-thickness puck, N_{zz} will be nonuniform, and this will make μ and κ also nonuniform, through Eqs. (4) and (5). Therefore we see that the circulator problem must by necessity become an inhomogeneous boundary value and forcing function problem. In those situations where a large enough bias field is applied to create saturation, $H_{ap} \approx H_{de}$ and their cancellation in Eq. (10) leads to $H_{i(ap)} \approx 0$. By Eq. (9), the net internal magnetic field H_i will be either $H_i \approx 0$ (ordinary ferrite material) or $H_i \approx H_{an}$ (hexagonal ferrite material). In fact, in a hexagonal ferrite, with $H_{ap} = 0$ and its remanent magnetization $M = 0$, we have $H_{i(ap)} = 0$ and $H_i = H_{an}$ holds exactly. Real hexagonal ferrites will have nonzero M, making $H_i = H_{an} - H_{de} \approx H_{an}$. For hexagonal ferrites where no applied magnetic field is necessary, typical anisotropy values of 17,000 Oe to 19,500 Oe lead to a ferromagnetic frequency range f_0 ($= \omega_0/2\pi$) from 47.6 GHz to 54.6 GHz. The anisotropy field is derived from the anisotropy energy of the ferrite. It produces a torque on the magnetization in the same manner as an externally applied field, and lies in the same direction as the remanent magnetization.

One of the issues that must be understood is why these devices are not operated near or at the ferromagnetic resonance frequency. Besides the intuitive idea that near-resonance operation may accentuate electromagnetic field loss due to absorption mechanisms, a simple rigorous way to see that this is indeed the case is to examine Eqs. (4) and (5) in the limit of low but finite α_m. Four reduced relationships are found for μ', μ'', κ', and κ'':

$$\mu' = 1 + \frac{\omega_m\omega_0}{\omega_0^2 - \omega^2} \tag{15a}$$

$$\mu'' = \frac{\omega_m\omega\alpha_m(\omega_0^2 + \omega^2)}{(\omega_0^2 - \omega^2)^2} \tag{15b}$$

$$\kappa' = -\frac{\omega_m\omega}{\omega_0^2 - \omega^2} \tag{16a}$$

$$\kappa'' = -\frac{2\omega_0\omega^2\alpha_m\omega_m}{(\omega_0^2 - \omega^2)^2} \tag{16b}$$

These expressions are accurate to first order in α_m. As $\omega \to \omega_0$, making the denominators in the loss component formulas for μ'' and κ'' approach zero, a second-order singularity is reached, namely $(\omega - \omega_0)^{-2}$, because

$$\lim_{\omega\to\omega_0} \frac{1}{(\omega_0^2-\omega^2)^2} = \lim_{\omega\to\omega_0} \frac{1}{(\omega_0-\omega)^2(\omega_0+\omega)^2} = \frac{1}{2\omega(\omega_0-\omega)^2} \tag{17}$$

This is precisely what makes it unacceptable to operate near the ferromagnetic resonance frequency. The strength of the singularity is first order in α_{m}.

Equations (15) and (16) may be used to assess the degree of circulation possible, which depends upon the amount of nonreciprocal anisotropy present in the ferrite material used in the device. Nonreciprocal anisotropy is measured by the ratio of the real part of the diagonal permeability to the real part of the off-diagonal permeability, κ'/μ'. Invoking Eqs. (15a) and (16a),

$$\frac{\kappa'}{\mu'} = -\frac{\omega_{\mathrm{m}}\omega}{\omega_0^2-\omega^2+\omega_{\mathrm{m}}\omega_0} \tag{18}$$

For $\omega_0 \approx 0$, the formula approaches

$$\lim_{\omega_0\to 0} \frac{\kappa'}{\mu'} = \frac{\omega_{\mathrm{m}}}{\omega} \tag{19}$$

This formula implies that it is necessary to have a sizable ω_{m} in order to obtain sizable circulation behavior, and this means a large magnetization value. In addition, bandwidth of a well-designed circulator can be shown to be roughly equal to ω_{m}, so there is a second reason for wanting large values of magnetization.

If $\omega \ll \omega_0$, the formula becomes

$$\lim_{\omega\ll\omega_0} \frac{\kappa'}{\mu'} = -\frac{\omega_{\mathrm{m}}\omega}{\omega_0(\omega_0+\omega_{\mathrm{m}})} \tag{20}$$

which further reduces if $\omega_{\mathrm{m}} \ll \omega_0$ to

$$\lim_{\omega,\omega_{\mathrm{m}}\ll\omega_0} \frac{\kappa'}{\mu'} = -\frac{\omega_{\mathrm{m}}\omega}{\omega_0^2} \tag{21}$$

In the limits of extremely high operating frequency ($\omega \to \infty$) or extremely high ferromagnetic resonance frequency ($\omega_0 \to \infty$), we use, respectively, Eqs. (19) and (21) to find

$$\lim_{\omega\to\infty,\omega_0\to 0} \frac{\kappa'}{\mu'} = \lim_{\omega\to\infty} \frac{\omega_{\mathrm{m}}}{\omega} = 0 \tag{22}$$

$$\lim_{\omega\to\infty,\omega_0\gg\omega} \frac{\kappa'}{\mu'} = -\lim_{\omega_0\to\infty} \frac{\omega_{\mathrm{m}}\omega}{\omega_0^2} = 0 \tag{23}$$

The extreme limiting cases $\omega \to \infty$ and $\omega_0 \to \infty$ can be found directly from Eq. (18). They tell us something about the actual cases of ferrite material made out of yttrium iron garnet (YIG) or a hexagonal ferrite such as BaM or SrM (M stands for $Fe_{12}O_{19}$). For YIG, where Eq. (22) applies, it is noticed that no circulation behavior can be utilized at very high frequencies. Therefore, for YIG, operation above the ferromagnetic resonance is required, but not so high as to cause nonreciprocity to be lost. But the diameter of a circulator is constrained to be approximately half the wavelength λ_{f} in the ferrite medium, because the puck acts (excluding the effects of the ports) as a distributed resonator; so this means that the operating resonance or electrical resonance must be above, but not too far above, the ferromagnetic resonance. Equation (23) applies to hexagonal material if the device is being operated far below the ferromagnetic resonance, and says that no circulation behavior will be found. Therefore, for BaM or SrM, operation below the ferromagnetic resonance is acceptable, but not so far below that nonreciprocity is lost. Because ω_0 is finite, on the order of 50 GHz, operation above the ferromagnetic resonance is possible too, and here the applicable limiting formula will be Eq. (22). Again, operation too far above this resonant point is not recommended, as useful nonreciprocity will quickly be lost.

The wavelength λ_{f} in the ferrite medium is calculated using the effective two-dimensional permeability

$$\mu_{\mathrm{eff}} = \mu\left[1-\left(\frac{\kappa}{\mu}\right)^2\right] \tag{24}$$

where the dependence on the ratio κ/μ is evident. From Eq. (24), the ferrite wavelength is calculated as

$$\lambda_{\mathrm{f}} = \frac{c}{f}\frac{1}{\sqrt{\epsilon_{\mathrm{f}}\mu_{\mathrm{eff}}}}, \qquad c = \frac{1}{\sqrt{\epsilon_0\mu_0}} \tag{25}$$

where relative values are used in the first formula and the second defines the free space velocity of light. An X-band circulator is typically 4 mm to 5 mm in diameter, and millimeter-wave devices are typically 1 mm or less, depending upon the dielectric constant of the ferrite and the operating frequency. Examination of the impedance as a function of diameter shows that whereas microwave circulators will have values below 20 Ω, millimeter-wave devices can be designed to have values close to 50 Ω.

Static Internal Magnetic Field

In developing electromagnetic radio frequency (RF) field solutions for circulators, the simplest assumption for the dc bias magnetic field is that of a nonvarying or constant spatial field. This may be satisfactory in many cases where the bias field circuit has been engineered to meet this requirement—particularly in the construction of permanent magnets for industrial applications, which is in a mature state of development, especially for low-frequency use. But this probably is not the case in hybrid or monolithic circuit applications for the microwave and millimeter-wave frequencies. Where laboratory measurements are conducted using large electromagnet pole pieces, the attainment of nearly constant magnetic field inside the pole pieces is assured. Such an arrangement is not possible, however, for a packaged miniaturized circulator with a nonideal geometrical configuration of the ferrite puck, permanent magnet, and flux return path. Even if the applied magnetic field is maintained uniform, the internal magnetic field H_{i}, which determines the values of the elements in the permeability tensor, will still not be uniform (except in the extreme limit of infinitesimal substrate thickness). Instead, the circulator's aspect ratio of radius to thickness controls the degree to which the inhomogeneous demagnetization field opposes the applied magnetic field.

One consequence of H_i variation is that the ferromagnetic resonance frequency, where the magnetic dissipation losses are a maximum, is spread out over a distribution of frequencies. For ordinary circulators designed with the ferromagnetic resonance frequency well below the geometrical shield RF resonant frequency (which approximates the center frequency of the circulator operating band), cancellation of the applied bias field by saturated magnetization leads to nearly zero H_i. Inhomogeneous demagnetization, however, can create a range of ferromagnetic resonance frequencies that are not zero and may become quite large close to the circulator perimeter, where H_i can rise dramatically. Thus near the circulator perimeter, the ferromagnetic resonance may encroach on the low-frequency end of the operating bandwidth, bringing many problems, including large losses to the outermost annular region.

H_i can be found by a direct self-consistent solution of Maxwell's magnetostatic (time-independent) equations, replacing the approximate demagnetization approach presented earlier. The relevant equation is the curl $\boldsymbol{H}$ relation, Ampere's law governing the magnetic field $\boldsymbol{H}$ in a current free, time-independent environment:

$$\nabla \times \boldsymbol{H} = 0 \tag{26}$$

Equation (26) is solved by specifying $\boldsymbol{H}$ as the gradient of a magnetostatic potential Ψ:

$$\boldsymbol{H} = -\nabla\psi \tag{27}$$

For nonlinear ferrite material, the constitutive relation is

$$\boldsymbol{B} = \mu_f(\boldsymbol{H} + \boldsymbol{M}) = \mu_0(\boldsymbol{H} + \boldsymbol{M}) \tag{28}$$

in MKS units, where the second equality comes about from the near-equality of μ_f and μ_0. In CGS units this relationship would have a factor 4π multiplying $\boldsymbol{M}$. In either case, $\boldsymbol{M}$ is the magnetization inside the ferrite material caused by the applied field $\boldsymbol{H}$, where we have dropped the earlier subscripts ($\boldsymbol{H}_{ap}$) for brevity. Note that the terms within parentheses are the resulting internal field [see Eqs. (10) and (11)]. For ordinary ferrites, the $\boldsymbol{B}$–$\boldsymbol{H}$ relation can be assumed to be single-valued because the hysteresis effect is small, and where it is most noticeable, near zero applied field, it is ignored. Such an assumption is not permissible for hexagonal ferrites, because they have a large anisotropy field (between 10,000 Oe and 30,000 Oe), which must be taken into account by Eq. (9), and have very hysteretic $\boldsymbol{B}$–$\boldsymbol{H}$ curves.

In any event, working with ordinary ferrite materials, where the single-valued nature of the $\boldsymbol{B}$–$\boldsymbol{H}$ relationship is accepted, the magnetic flux density $\boldsymbol{B}$ is a nonlinear, monotonically increasing function of $\boldsymbol{H}$ and in the same direction as $\boldsymbol{H}$. The magnetization $\boldsymbol{M}$ is incorporated into a nonlinear permeability factor $\mu(H)$, where H is the field magnitude, yielding

$$\boldsymbol{B} = \mu(H)\boldsymbol{H} \tag{29}$$

Since the divergence of $\boldsymbol{B}$ is zero,

$$\nabla \cdot \boldsymbol{B} = 0 \tag{30}$$

in the previous $\boldsymbol{B}$ expression, one finds the nonlinear Poisson equation for the magnetostatic potential as in Newman and Krowne (3):

$$\nabla \cdot [\mu(|\nabla\Psi|)\,\nabla\Psi] = 0 \tag{31}$$

Expanding this formula gives

$$\mu(|\nabla\Psi|)\,\nabla^2\Psi + \nabla\mu(|\nabla\Psi|)\cdot\nabla\Psi = 0 \tag{32}$$

or

$$\nabla^2\Psi + \frac{1}{\mu(|\nabla\Psi|)}\nabla\mu(|\nabla\Psi|)\cdot\nabla\Psi = 0 \tag{33}$$

Any of the forms in Eqs. (31) to (33) may be solved for Ψ.

The magnetostatic potential (and as a result, the demagnetizing field) is conveniently solved in the cylindrical coordinate system, consistent with a circular ferrite puck cross section. Nonlinear Poisson Eq. (31) becomes

$$\frac{1}{r}\frac{\partial}{\partial r}\left(r\mu(|\nabla\Psi|)\frac{\partial\Psi}{\partial r}\right) + \frac{1}{r}\frac{\partial}{\partial\phi}\left(\mu(|\nabla\Psi|)\frac{\partial\Psi}{\partial\phi}\right) + \frac{\partial}{\partial z}\left(\mu(|\nabla\Psi|)\frac{\partial\Psi}{\partial z}\right) = 0 \tag{34}$$

Because of the azimuthal (ϕ) symmetry, the three-dimensional puck region problem reduces to a 2-D problem in the coordinates r, z:

$$\frac{1}{r}\frac{\partial}{\partial r}\left(r\mu(|\nabla\Psi|)\frac{\partial\Psi}{\partial r}\right) + \frac{\partial}{\partial z}\left(\mu(|\nabla\Psi|)\frac{\partial\Psi}{\partial z}\right) = 0 \tag{35}$$

Equation (35) has a singularity at the origin, which is removable by multiplying through by r, giving the well-posed problem equation

$$\frac{\partial}{\partial r}\left(r\mu(|\nabla\Psi|)\frac{\partial\Psi}{\partial r}\right) + \frac{\partial}{\partial z}\left(r\mu(|\nabla\Psi|)\frac{\partial\Psi}{\partial z}\right) = 0 \tag{36}$$

The magnitude of the gradient of the scalar magnetostatic potential Ψ in Eq. (36) is

$$|\nabla\Psi| = \left[\left(\frac{\partial\Psi}{\partial r}\right)^2 + \left(\frac{\partial\Psi}{\partial z}\right)^2\right]^{1/2} \tag{37}$$

Recalling Eq. (27), the z-directed component of the dc magnetic field used to provide bias for the ac RF problem is obtained from the above solution as

$$H_z = -\frac{\partial\Psi}{\partial z} \tag{38}$$

The puck volume is contained within the region $0 \le r \le a$, $0 \le z \le 2h$, and $0 \le \phi \le 2\pi$. Using an rz cutting plane reduces the 3-D problem to one of two dimensions, and symmetry further simplifies it to the rectangular domain $0 \le r \le L_r$ and $0 \le z \le L_z$. In the final reduced domain, the ferrite material occupies the region $0 \le r \le a$ and $0 \le z \le h$. The problem is solved for the case when an external magnetic field $\boldsymbol{H}_{ap} = H_{ap}\hat{z}$ is applied; that is, when the puck is removed, only a uniform field exists in the z direction. Therefore, we require, far from the puck (say at $z = L_z$), that the gradient of the magnetostatic potential Ψ normal to the boundary only be in the z direction and have a value

$$\frac{\partial \Psi}{\partial z} = -H_{\mathrm{ap}}, \qquad z = L_z \text{ and } 0 \le r \le L_r \tag{39}$$

At the center of the puck, due to symmetry (midline $r = 0$, $0 \le z \le L_z$), and on the outside circumference ($r = L_r$, $0 \le z \le L_z$) of the puck and far from it, the magnetostatic potential normal to the boundary has zero value (zero r-directed field), so that

$$\frac{\partial \Psi}{\partial r} = 0, \qquad r = 0 \text{ and } 0 \le z \le L_z \tag{40}$$

$$\frac{\partial \Psi}{\partial r} = 0, \qquad r = L_r \text{ and } 0 \le z \le L_z \tag{41}$$

Finally, at the midplane ($r\phi$ plane) of the puck, the gradient of the magnetostatic potential Ψ parallel to the boundary ($z = 0$, $0 \le r \le L_r$) must be zero due to symmetry (zero r-directed field):

$$\frac{\partial \Psi}{\partial r} = 0, \qquad z = 0, \quad 0 \le r \le L_r \tag{42}$$

Integration of Eq. (40) yields

$$\Psi = \text{constant}, \qquad z = 0, \quad 0 \le r \le L_r \tag{43}$$

and because of superposition and the gradient nature of the magnetic field, this constant is arbitrary and so may be set to zero.

The permeability function $\mu(H)$ is constructed as follows. Outside the puck, $\mu(H) = \mu_0$. Inside the puck, it is required that the permeability function be single-valued, necessitating neglect of hysteresis. A reasonable and convenient analytical approximation developed for $\mu(H)$ is given in Newman and Krowne (3) as

$$\mu(H) = \mu_0 \left(1 + \frac{M_{\mathrm{s}}}{\sqrt{H_1^2 + H^2}}\right) \tag{44}$$

M_{s} is the saturation magnetization, and H_1 is the corner magnetic field, at which the magnetization reaches 0.707 times its saturation value. The corner field H_1 is often on the order of 1 Oe, and at that field the magnetic flux density $\boldsymbol{B}$ is on the order of but still much less than the saturation magnetization, which is often on the order of thousands of gauss. An advantage of the ferrite model (44) over a piecewise linear model is that it is continuous, producing continuous Jacobian matrix elements that can be calculated explicitly in a numerical procedure.

UNIFORM TWO-DIMENSIONAL GREEN'S FUNCTION

Simplest case to treat is that of a uniform ferrite material in the puck (see Fig. 1), and this leads to what is referred to as the uniform Green's function solution. Uniform Green's function solution is found assuming that perfect magnetic walls for arcs connecting port apertures. That case may also be referred to as the *hard wall* case, since electromagnetic waves cannot propagate through the interfacial arcs separating the ferrite and external dielectric regions.

Two-Dimensional Hard Wall Case

The uniform 2-D Green's function for the hard wall situation is

$$G_{\mathrm{un}}(\phi, \phi_{\mathrm{q}}) = \frac{i\zeta_{\mathrm{eff}}}{2\pi} \sum_{n=-\infty}^{\infty} \frac{J_n(k_{\mathrm{eff}} r)}{J_n'(k_{\mathrm{eff}} r) - \dfrac{\kappa}{\mu} \dfrac{n}{k_{\mathrm{eff}} r} J_n(k_{\mathrm{eff}} r)} e^{in(\phi - \phi_{\mathrm{q}})} \tag{45}$$

where the effective impedance coefficient is given by

$$\zeta_{\mathrm{eff}} = \frac{\omega \mu_0 \mu_{\mathrm{eff}}}{k_{\mathrm{eff}}} \tag{46}$$

This is precisely Bosma's (1) uniform Green's function solution relating one angular source point located at ϕ_{q} to the response point located at ϕ when specializing to the perimeter $r = R$. Equation (45) on the right-hand side for G_{un} is given in abbreviated notation, and hides the fact that this Green's function does not have to be specialized to the contour circulator perimeter (where $r = R$) and that it only relates the driving magnetic field source H to the resulting electric field E. Furthermore, it only relates an azimuthal magnetic field source (ϕ component) to a perpendicular electric field response (z component). So in reality, Eq. (45) represents only one dyadic element of a complete dyadic Green's function. Properly stated in explicit general form, the uniform Green's function is written

$$G_{EH,\mathrm{un}}^{z\phi}(r, \phi; R, \phi_{\mathrm{q}}) = \frac{i\zeta_{\mathrm{eff}}}{2\pi} \sum_{n=-\infty}^{\infty} \frac{J_n(k_{\mathrm{eff}} r)}{J_n'(k_{\mathrm{eff}} r) - \dfrac{\kappa}{\mu} \dfrac{n}{k_{\mathrm{eff}} r} J_n(k_{\mathrm{eff}} r)} e^{in(\phi - \phi_{\mathrm{q}})} \tag{47}$$

This may be put into a much more compact form if the product of part of the summation prefactor and the radial part of the summand is defined as

$$\overline{\gamma}_{n0}^{z\phi} = i\zeta_{\mathrm{eff}} \frac{J_n(k_{\mathrm{eff}} r)}{J_n'(k_{\mathrm{eff}} r) - \dfrac{\kappa}{\mu} \dfrac{n}{k_{\mathrm{eff}} r} J_n(k_{\mathrm{eff}} r)} \tag{48}$$

One obtains from Eq. (47), using Eq. (48),

$$G_{EH,\mathrm{un}}^{z\phi}(r, \phi; R, \phi_{\mathrm{q}}) = \frac{1}{2\pi} \sum_{n=-\infty}^{\infty} \overline{\gamma}_{n0}^{z\phi} e^{in(\phi - \phi_{\mathrm{q}})} \tag{49}$$

Two-Dimensional Soft Wall Case

If it is desired to find some way of determining the effect of the external dielectric region on the circulator behavior, the perfect magnetic walls must be replaced by penetrable walls. A dyadic Green's function allowing for such *soft wall* (as opposed to hard wall) conditions enables us to find out the effect of changes in the permittivity ϵ_{d} and permeability μ_{d} on circulator performance. The three common cases of air as the external medium, a dielectric as the external medium, and an unmagnetized ferrite as the external medium are all easy to treat with the soft wall dyadic Green's function.

Applying the radiation condition as $r \to \infty$ leads to the selection of the modified Bessel function of the second kind, $K_n(k_d r)$, for use in the external field construction, $r > R$. It is assumed that the same field modes are maintained in the device for radii exceeding the circulator radius, so that a consistent 2-D modeling procedure holds inside and outside the device. Additionally, the contribution of the microstrip edge effect and fringing field provides the correct field available from the circulator puck for coupling to the external environment when multiplied by the factor f. How to find f is discussed in Krowne (4). With these constraints, the internal TM_z nature of the field persists for $r > R$, whence

$$E_z^{\mathrm{d}} = \sum_{n=-\infty}^{\infty} a_{n\mathrm{e}}^{\mathrm{d}} K_n(k_{\mathrm{d}} r) e^{in\phi} \tag{50}$$

$$H_\phi^{\mathrm{d}} = \frac{1}{i\omega\mu_{\mathrm{d}}} \sum_{n=-\infty}^{\infty} a_{n\mathrm{e}}^{\mathrm{d}} k_{\mathrm{d}} K_n'(k_{\mathrm{d}} r) e^{in\phi} \tag{51}$$

Continuity of the perpendicular electric field at $r = R$ is required:

$$f E_z^{\mathrm{c}}(R, \phi) = E_z^{\mathrm{d}}(R, \phi) \tag{52}$$

This gives

$$a_{n\mathrm{e}}^{\mathrm{d}} = f \frac{J_n(k_{\mathrm{e}} R)}{K_n(k_{\mathrm{d}} R)} a_{n0} \tag{53}$$

where

$$k_{\mathrm{d}} = \omega\sqrt{\epsilon_{\mathrm{d}}\mu_{\mathrm{d}}} \tag{54}$$

f attempts in an approximate way to allow for consistent fringing in the 2-D model, which has some inherent degree of 3-D nature.

The forcing function for the Green's function is applied at (r', ϕ'), $r = R$, through the equality

$$H_\phi^{\mathrm{Per}}(R, \phi) = H_{\phi'\mathrm{A}} \delta(\phi - \phi')\, \Delta\phi' + H_\phi^{\mathrm{d}}(R, \phi \neq \phi') \tag{55}$$

Obtaining solution of internal puck amplitude coefficient a_{n0} in terms of the forcing field $H_{\phi'\mathrm{A}}$, the elements of the dyadic Green's function for $r < R$ (within the circulator puck) may be written as

$$G_{EH}^{z\phi}(r, \phi; R, \phi') = \frac{i\omega}{2\pi} \sum_{n=-\infty}^{\infty} \frac{J_n(k_{\mathrm{e}} r) e^{in(\phi-\phi')}}{\dfrac{1}{\mu_{\mathrm{e}}}\left(k_{\mathrm{e}} J_n'(k_{\mathrm{e}} R) - \dfrac{n\kappa}{\mu}\dfrac{1}{R} J_n(k_{\mathrm{e}} R)\right) - f \dfrac{k_{\mathrm{d}}}{\mu_{\mathrm{d}}} \dfrac{J_n(k_{\mathrm{e}} R)}{K_n(k_{\mathrm{d}} R)} K_n'(k_{\mathrm{d}} R)} \tag{56}$$

$$G_{HH}^{\phi\phi}(r, \phi; R, \phi') = \frac{1}{2\pi} \sum_{n=-\infty}^{\infty} \frac{\left(J_n'(k_{\mathrm{e}} r) - \dfrac{n\kappa}{\mu}\dfrac{1}{k_{\mathrm{e}} r} J_n(k_{\mathrm{e}} r)\right) e^{in(\phi-\phi')}}{J_n'(k_{\mathrm{e}} R) - \dfrac{n\kappa}{\mu}\dfrac{1}{k_{\mathrm{e}} R} J_n(k_{\mathrm{e}} R) - f \dfrac{\mu_{\mathrm{e}}}{\mu_{\mathrm{d}}} \dfrac{k_{\mathrm{d}}}{k_{\mathrm{e}}} \dfrac{J_n(k_{\mathrm{e}} R)}{K_n(k_{\mathrm{d}} R)} K_n'(k_{\mathrm{d}} R)} \tag{57}$$

$$G_{HH}^{r\phi}(r, \phi; R, \phi') = \frac{i}{2\pi} \sum_{n=-\infty}^{\infty} \frac{\left(\dfrac{n}{k_{\mathrm{e}} r} J_n(k_{\mathrm{e}} r) - \dfrac{\kappa}{\mu} J_n'(k_{\mathrm{e}} r)\right) e^{in(\phi-\phi')}}{J_n'(k_{\mathrm{e}} R) - \dfrac{n\kappa}{\mu}\dfrac{1}{k_{\mathrm{e}} R} J_n(k_{\mathrm{e}} R) - f \dfrac{\mu_{\mathrm{e}}}{\mu_{\mathrm{d}}} \dfrac{k_{\mathrm{d}}}{k_{\mathrm{e}}} \dfrac{J_n(k_{\mathrm{e}} R)}{K_n(k_{\mathrm{d}} R)} K_n'(k_{\mathrm{d}} R)} \tag{58}$$

For $r > R$ (outside the circulator puck), the dyadic Green's function elements are

$$G_{EH}^{z\phi}(r, \phi; R, \phi') = \frac{i\omega f}{2\pi} \sum_{n=-\infty}^{\infty} \frac{\dfrac{J_n(k_{\mathrm{e}} R)}{K_n(k_{\mathrm{d}} R)} K_n(k_{\mathrm{d}} r) e^{in(\phi-\phi')}}{\dfrac{1}{\mu_{\mathrm{e}}}\left(k_{\mathrm{e}} J_n'(k_{\mathrm{e}} R) - \dfrac{n\kappa}{\mu}\dfrac{1}{R} J_n(k_{\mathrm{e}} R)\right) - f \dfrac{k_{\mathrm{d}}}{\mu_{\mathrm{d}}} \dfrac{J_n(k_{\mathrm{e}} R)}{K_n(k_{\mathrm{d}} R)} K_n'(k_{\mathrm{d}} R)} \tag{59}$$

$$G_{HH}^{\phi\phi}(r, \phi; R, \phi') = \frac{\mu_{\mathrm{e}}}{\mu_{\mathrm{d}}} \frac{k_{\mathrm{d}}}{k_{\mathrm{e}}} f \frac{1}{2\pi} \sum_{n=-\infty}^{\infty} \frac{\dfrac{J_n(k_{\mathrm{e}} R)}{K_n(k_{\mathrm{d}} R)} K_n'(k_{\mathrm{d}} r) e^{in(\phi-\phi')}}{J_n'(k_{\mathrm{e}} R) - \dfrac{n\kappa}{\mu}\dfrac{1}{k_{\mathrm{e}} R} J_n(k_{\mathrm{e}} R) - f \dfrac{\mu_{\mathrm{e}}}{\mu_{\mathrm{d}}} \dfrac{k_{\mathrm{d}}}{k_{\mathrm{e}}} \dfrac{J_n(k_{\mathrm{e}} R)}{K_n(k_{\mathrm{d}} R)} K_n'(k_{\mathrm{d}} R)} \tag{60}$$

$$G_{HH}^{r\phi}(r, \phi; R, \phi') = -n \frac{\mu_{\mathrm{e}}}{\mu_{\mathrm{d}}} k_{\mathrm{e}} \frac{f}{r} \frac{i}{2\pi} \sum_{n=-\infty}^{\infty} \frac{\dfrac{J_n(k_{\mathrm{e}} R)}{K_n(k_{\mathrm{d}} R)} K_n(k_{\mathrm{d}} r) e^{in(\phi-\phi')}}{J_n'(k_{\mathrm{e}} R) - \dfrac{n\kappa}{\mu}\dfrac{1}{k_{\mathrm{e}} R} J_n(k_{\mathrm{e}} R) - f \dfrac{\mu_{\mathrm{e}}}{\mu_{\mathrm{d}}} \dfrac{k_{\mathrm{d}}}{k_{\mathrm{e}}} \dfrac{J_n(k_{\mathrm{e}} R)}{K_n(k_{\mathrm{d}} R)} K_n'(k_{\mathrm{d}} R)} \tag{61}$$

The factor f is estimated as $f = f_{\mathrm{w}} f_{\mathrm{p}}$, where f_{w} weights the parameter dependence expression in f_{p}. Closed-form formulas, based upon self-consistent static solutions, exist for microstrip capacitive (electric) end effects. Stretching the microstrip end so as to connect one corner to the other constructs the circulator perimeter, and allows us to roughly obtain f_{p}:

$$f_{\mathrm{p}} = \frac{C_{\mathrm{T}} - C}{C} = \frac{C_{\mathrm{f}}}{C} = \frac{h}{A\epsilon_{\mathrm{d}}} C_{\mathrm{f}} \tag{62}$$

Assign $A = \pi R^2$ and $W = 2\pi R$, and place them in Eq. (62) and in the equivalent expression for the additional radial length Δl_{f}, which relates to the fringing capacitance C_{f}:

$$\frac{\Delta l_{\mathrm{f}}}{h} = \frac{C_{\mathrm{f}}}{W} \frac{c Z_{\mathrm{m}} W/h}{\sqrt{\epsilon_{\mathrm{rde}}}} \tag{63}$$

where c is the speed of light in vacuum, h the substrate thickness, Z_{m} the microstrip impedance based on dielectric ϵ_{d} loading causing an effective dielectric constant ϵ_{de}, and the subscript r denotes relative value. We replace ϵ_{de} by ϵ_{d} in the limit $W/h \gg 1$. The left-hand side of Eq. (63) is given by

$$\frac{\Delta l_{\mathrm{f}}}{h} = 0.412 \frac{\epsilon_{\mathrm{rde}} + 0.300}{\epsilon_{\mathrm{rde}} - 0.258} \frac{W/h + 0.264}{W/h + 0.800} \tag{64}$$

Using Eqs. (63) and (64) in Eq. (62), the final formula for f is

$$f_{\mathrm{p}} = \frac{0.824h}{R\sqrt{\epsilon_{\mathrm{rd}}}} \frac{\epsilon_{\mathrm{rd}} + 0.300}{\epsilon_{\mathrm{rd}} - 0.258} \frac{R/h + 0.042}{R/h + 0.127} \times \left\{1 + \frac{h}{R}\left[0.2217 + 0.106 \ln\left(2\pi\frac{R}{h} + 1.444\right)\right]\right\} \tag{65}$$

We have assumed that the cover location $h' \gg h$ in deriving Eq. (65).

One would expect the prefactor f_w to contain information on the azimuthal mode structure, and this will be displayed as a dependence on the azimuthal mode index n. The prefactor f_w may be very complicated, and the best that one can do is to obtain some reasonable degree of approximation.

UNIFORM THREE-DIMENSIONAL GREEN'S FUNCTION

The big difference between the 2-D treatment and the 3-D treatment is that inclusion of finite puck thickness creates a perpendicular propagation constant k_z, and its existence makes the radial propagation constant split into two dissimilar values. Perfect magnetic walls are still maintained, however, on those segments of the circulator perimeter where ports do not exist. Electromagnetic fields now have variation in the perpendicular coordinate direction z. As a consequence, the field solution for the circulator is considerably complicated. Figure 1 still applies to a z = const plane cut through the height of the device.

Three-Dimensional Uniform Hard Wall Case

The transverse electromagnetic field components within the circulator can be expressed in terms of the perpendicular electric and magnetic field components. The circulator field E_z^c at its most extreme position $r = R$ is expressed using Krowne (5) as

$$E_z^c = \sum_{j=0}^{\infty} \sum_{n=-\infty}^{\infty} \cos(k_{zj}z)\,[a_{n0j}^1 J_n(\sigma_{1j}R) + a_{n0j}^2 J_n(\sigma_{2j}R)]e^{in\phi} \quad (66)$$

The perpendicular magnetic field in the circulator, as $r \to R$ from the inside, is given by

$$H_z^c = \sum_{j=1}^{\infty} \sum_{n=-\infty}^{\infty} i \sin(k_{zj}z) \left(a_{n0j}^1 \frac{c_j - \lambda_{2j}}{b_j} J_n(\sigma_{1j}R) + a_{n0j}^2 \frac{c_j - \lambda_{1j}}{b_j} J_n(\sigma_{2j}R) \right) e^{in\phi} \quad (67)$$

The circulator field E_ϕ^c at its most extreme position $r = R$ is expressed as

$$E_\phi^c = \sum_{j=1}^{\infty} \sum_{n=-\infty}^{\infty} i \sin(k_{zj}z) \times \left[a_{n0j}^1 \left(\frac{-in\bar{r}_j}{b_j R} \lambda_{2j} J_n(\sigma_{1j}R) + \frac{\sigma_{1j}}{b_j}(i\omega\mu_0 + s_j\lambda_{2j}) J_n'(\sigma_{1j}R) \right) + a_{n0j}^2 \left(\frac{-in\bar{r}_j}{b_j R} \lambda_{1j} J_n(\sigma_{2j}R) + \frac{\sigma_{2j}}{b_j}(i\omega\mu_0 + s_j\lambda_{1j}) J_n'(\sigma_{2j}R) \right) \right] e^{in\phi} \quad (68)$$

An azimuthal magnetic field in the circulator, as $r \to R$ from the inside, is given by

$$H_\phi^c = \sum_{j=0}^{\infty} \sum_{n=-\infty}^{\infty} \cos(k_{zj}z) \left\{ a_{n0j}^1 \left[\frac{in}{b_j R} \left(ik_z \frac{\mu_0}{\mu} - p_j\lambda_{2j} \right) J_n(\sigma_{1j}R) + \frac{q_j}{b_j} \lambda_{2j}\sigma_{1j} J_n'(\sigma_{1j}R) \right] + a_{n0j}^2 \left[\frac{in}{b_j R} \left(ik_z \frac{\mu_0}{\mu} - p_j\lambda_{1j} \right) \times J_n(\sigma_{2j}R) + \frac{q_j}{b_j} \lambda_{1j}\sigma_{2j} J_n'(\sigma_{2j}R) \right] \right\} e^{in\phi} \quad (69)$$

Working with the fields given by Eqs. (66) to (69) (replace R by r for the dependence within the puck) enables the hard wall dyadic Green's function to be found.

Three-Dimensional Uniform Soft Wall Case

With the assumption that the electric wall conditions are approximately maintained for radii exceeding the circulator radius, so that the same z-indexing modal set can be used inside and outside the device, the problem becomes tractable enough so that an explicit dyadic Green's function solution can be sought. Fields external to the puck in the dielectric region look like

$$E_z^d(r,\phi,z) = \sum_{j=0}^{\infty} \sum_{n=-\infty}^{\infty} a_{nej}^d \cos(k_{zj}z) K_n(\sigma_{dj}r) e^{in\phi} \quad (70)$$

$$H_z^d(r,\phi,z) = \sum_{j=1}^{\infty} \sum_{n=-\infty}^{\infty} i a_{nhj}^d \sin(k_{zj}z) K_n(\sigma_{dj}r) e^{in\phi} \quad (71)$$

Here the characteristic equation for the radial separation constant σ_{dj} is given in the outside region by (notice that it is single-valued)

$$\sigma_{dj} = \sqrt{k_d^2 - k_{zj}^2}, \qquad k_d = \omega\sqrt{\epsilon_d \mu_d} \quad (72)$$

where the perpendicular indexing for the discrete spectrum of allowed values is done according to

$$k_{zj} = \frac{j\pi}{h}, \qquad j = (0 \text{ or } 1), 2, \ldots \quad (73)$$

with the first j index choice determined by the first nontrivial field component.

The azimuthal magnetic field component H_ϕ^d (only the transverse part) may be made to retain a form congruent with the puck field construction, following Krowne (6), by setting the coefficient factors q and t of the partial differential operators $\partial/\partial r$ and $\partial/\partial\phi$ equal to zero:

$$H_\phi^d = \frac{p}{r}\frac{\partial H_z^d}{\partial \phi} - u\frac{\partial E_z^d}{\partial r} \quad (74)$$

with

$$p = \frac{ik_{zj}}{k_d^2 - k_{zj}^2}, \qquad u = \frac{i\omega\epsilon_d}{k_d^2 - k_{zj}^2} \quad (75)$$

Similarly, the azimuthal electric field component E_ϕ^d (only the transverse part) may be made to retain a form congruent with the puck field construction by setting the coefficient factors $\bar{r}$ and q of the partial differential operators $\partial/\partial\phi$ and $\partial/\partial r$ equal to zero:

$$E_\phi^d = -s\frac{\partial H_z^d}{\partial r} + \frac{p}{r}\frac{\partial E_z^d}{\partial \phi} \quad (76)$$

with

$$s = -\frac{i\omega\mu_d}{k_d^2 - k_{zj}^2} \quad (77)$$

The perpendicular magnetic field forcing function for the Green's function is applied at (r', ϕ'), $r = R$, through the equality

$$H_z^{\mathrm{Per}}(R,\phi) = H_{z\mathrm{A}} h(z)\delta(\phi-\phi')\,\Delta\phi' + H_z^{\mathrm{d}}(R,\,\phi\neq\phi') \tag{78}$$

Here $h(z)$ is the functional behavior of the forcing perpendicular magnetic field in the z direction. This relationship must be added to that in Eq. (55) to completely describe the source. Using the puck field forms given by Eqs. (66) to (69) and the external-region fields given by Eqs. (70), (71), (74), and (76) enables the soft wall dyadic Green's function to be found.

INHOMOGENEOUS TWO-DIMENSIONAL DYADIC GREEN'S FUNCTION

A new aspect of the inhomogeneous case is that the circulator puck has varying properties throughout its radial extent (see Fig. 2). Its magnetization, demagnetization factor, and applied magnetic bias field are all capable of changing with the radius. The Green's functions utilize recursive relationships between adjacent radial sections or rings to provide compact expressions, the actual algebraic factors contained inside the summations being extremely complicated.

Two-Dimensional Inhomogeneous Hard Wall Case

The dyadic Green's function elements are now given by the new expressions provided in Krowne (7):

$$G_{EHi}^{z\phi}(r,\phi;R,\phi_{\mathrm{k}}^{\mathrm{q}}) = \frac{1}{2\pi}\sum_{n=-\infty}^{\infty} \frac{a_{ni}(\mathrm{recur})C_{neai}(r) + b_{ni}(\mathrm{recur})C_{nebi}(r)}{\gamma_{n\mathrm{N}}} e^{-in\phi_k^q} e^{in\phi} \tag{79}$$

$$G_{HHi}^{\phi\phi}(r,\phi;R,\phi_{\mathrm{k}}^{\mathrm{q}}) = \frac{1}{2\pi}\sum_{n=-\infty}^{\infty} \frac{a_{ni}(\mathrm{recur})C_{nehi}^{\phi}(r) + b_{ni}(\mathrm{recur})C_{nhbi}^{\phi}(r)}{\gamma_{n\mathrm{N}}} e^{-in\phi_k^q} e^{in\phi} \tag{80}$$

$$G_{HHi}^{r\phi}(r,\phi;R,\phi_{\mathrm{k}}^{\mathrm{q}}) = \frac{1}{2\pi}\sum_{n=-\infty}^{\infty} \frac{a_{ni}(\mathrm{recur})C_{nhai}^{r}(r) + b_{ni}(\mathrm{recur})C_{nhbi}^{r}(r)}{\gamma_{n\mathrm{N}}} e^{-in\phi_k^q} e^{in\phi} \tag{81}$$

where

$$\gamma_{n\mathrm{N}} = \gamma_{n\mathrm{N}}^{\phi h} = a_{n\mathrm{N}}(\mathrm{recur})C_{nha\mathrm{N}}^{\phi}(R) + b_{n\mathrm{N}}(\mathrm{recur})C_{nhb\mathrm{N}}^{\phi}(R) \tag{82}$$

Notice that the radial variation of each dyadic Green's function element differs based on the numerator sum character inside the infinite summation changing from one element to another. The sum in each numerator is constructed from recursion coefficients a_{ni}(recur) and b_{ni}(recur), which give the correct coefficient in the ith ring after successive recursion processes have been performed on all previous annuli within the ferrite puck.

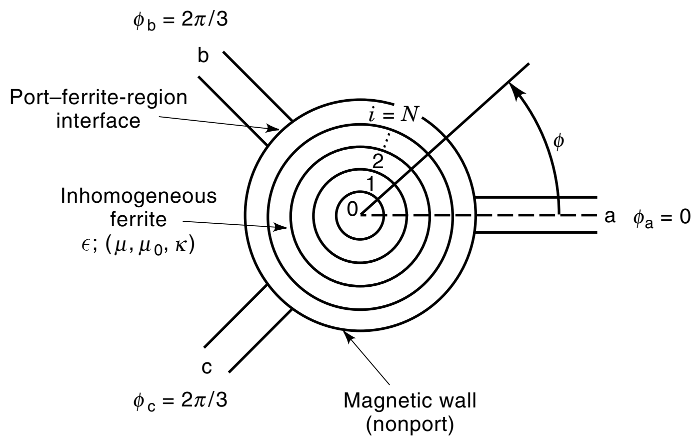

Figure 2. Top view (as in Fig. 1) of an inhomogeneous circulator. Within the perimeter is ferrite with radially varying parameters, broken up into N annuli, each uniform. Outside the perimeter are the ports (three here) and the external dielectric. Hard wall conditions require a magnetic wall as shown. Soft wall conditions necessitate its change to a penetrable inhomogeneous wall between two dissimilar materials.

If we assign a notation similar to that found in Eq. (82) to the radial numerator factors in Eqs. (79) to (81),

$$\gamma_{ni}^{ze}(r) = a_{ni}(\mathrm{recur})C_{nhai}^{z}(r) + b_{ni}(\mathrm{recur})C_{nhbi}^{z}(r) \tag{83}$$

$$\gamma_{ni}^{\phi h}(r) = a_{ni}(\mathrm{recur})C_{nhai}^{\phi}(r) + b_{ni}(\mathrm{recur})C_{nhbi}^{\phi}(r) \tag{84}$$

$$\gamma_{ni}^{rh}(r) = a_{ni}(\mathrm{recur})C_{nhai}^{r}(r) + b_{ni}(\mathrm{recur})C_{nhbi}^{r}(r) \tag{85}$$

and define normalized quantities

$$\overline{\gamma}_{ni}^{pq}(r) = \frac{\gamma_{ni}^{pq}(r)}{\gamma_{n\mathrm{N}}^{\phi h}(R)} \tag{86}$$

then the dyadic Green's function elements given in Eqs. (79) to (81) can be streamlined. Here $p = z, \phi, r$ and $q = e, h$.

Final compacted forms for the 2-D hard wall dyadic Green's function elements are

$$G_{EHi}^{z\phi}(r,\phi;R,\phi_k^q) = \frac{1}{2\pi}\sum_{n=-\infty}^{\infty} \overline{\gamma}_{ni}^{ze}(r) e^{in(\phi-\phi_k^q)} \tag{87}$$

$$G_{HHi}^{\phi\phi}(r,\phi;R,\phi_k^q) = \frac{1}{2\pi}\sum_{n=-\infty}^{\infty} \overline{\gamma}_{ni}^{\phi h}(r) e^{in(\phi-\phi_k^q)} \tag{88}$$

$$G_{HHi}^{r\phi}(r,\phi;R,\phi_k^q) = \frac{1}{2\pi}\sum_{n=-\infty}^{\infty} \overline{\gamma}_{ni}^{rh}(r) e^{in(\phi-\phi_k^q)} \tag{89}$$

The indexing of the azimuthal angle ϕ has to do with identifying the location of the port q and the discretization within each port k. One can see from this discussion that the final form of the $z\phi$ element is precisely the same as for the uniform case in Eq. (49). This is no coincidence. Compacting the recursion process and the separable property of the partial differential equation describing electromagnetic waves within the circulator enables the inhomogeneous problem solution to be developed in this manner.

Two-Dimensional Inhomogeneous Soft Wall Case

Like the hard wall case, inhomogeneity complicates the electromagnetic problem, but with the techniques of compacting the recursion process, the dyadic Green's function elements are now given by the formulas

$$G^{z\phi}_{EHi}(r,\phi;R,\phi') = \frac{1}{2\pi}\sum_{n=-\infty}^{\infty} \frac{a_{ni}(\text{recur})C_{neai}(r) + b_{ni}(\text{recur})C_{nebi}(r)}{\gamma_{nN} - \dfrac{fk_{\text{d}}}{i\omega\mu_{\text{d}}}\dfrac{\gamma^{ze}_{n\text{N}}}{K_n(k_{\text{d}}R)}K'_n(k_dR)} e^{in(\phi-\phi')} \tag{90}$$

$$G^{\phi\phi}_{HHi}(r,\phi;R,\phi') = \frac{1}{2\pi}\sum_{n=-\infty}^{\infty} \frac{a_{ni}(\text{recur})C^{\phi}_{nhai}(r) + b_{ni}(\text{recur})C^{\phi}_{nhbi}(r)}{\gamma_{nN} - \dfrac{fk_{\text{d}}}{i\omega\mu_{\text{d}}}\dfrac{\gamma^{ze}_{n\text{N}}}{K_n(k_{\text{d}}R)}K'_n(k_dR)} e^{in(\phi-\phi')} \tag{91}$$

$$G^{r\phi}_{HHi}(r,\phi;R,\phi') = \frac{1}{2\pi}\sum_{n=-\infty}^{\infty} \frac{a_{ni}(\text{recur})C^{r}_{nhai}(r) + b_{ni}(\text{recur})C^{r}_{nhbi}(r)}{\gamma_{nN} - \dfrac{fk_{\text{d}}}{i\omega\mu_{\text{d}}}\dfrac{\gamma^{ze}_{n\text{N}}}{K_n(k_{\text{d}}R)}K'_n(k_dR)} e^{in(\phi-\phi')} \tag{92}$$

It is evident comparing Eqs. (90) to (92) with Eqs. (79) to (81) that the new dyadic Green's function elements are those of a circulator device with hard walls (namely magnetic walls), but with a modification to the form of the denominator. This modification is in the form of a subtraction from the original circulator divisor $\gamma_{n\text{N}}$, and depends on the properties of the external medium, on the internal circulator field behavior through $\gamma^{ze}_{n\text{N}}$, and on the factor f.

The elements of the dyadic Green's function external to the circulator, in the nonport regions, are

$$G^{z\phi}_{EH\text{d}}(r,\phi;R,\phi') = \frac{1}{2\pi}\sum_{n=-\infty}^{\infty} \frac{f\gamma^{ze}_{n\text{N}}}{K_n(k_{\text{d}}R)} \frac{K_n(k_{\text{d}}r)}{\gamma_{nN} - \dfrac{fk_{\text{d}}}{i\omega\mu_{\text{d}}}\dfrac{\gamma^{ze}_{n\text{N}}}{K_n(k_{\text{d}}R)}K'_n(k_{\text{d}}R)} e^{in(\phi-\phi')} \tag{93}$$

$$G^{\phi\phi}_{HH\text{d}}(r,\phi;R,\phi') = \frac{1}{2\pi}\sum_{n=-\infty}^{\infty} \frac{fk_{\text{d}}}{i\omega\mu_{\text{d}}}\frac{\gamma^{ze}_{n\text{N}}}{K_n(k_{\text{d}}R)} \frac{K'_n(k_{\text{d}}r)}{\gamma_{n\text{N}} - \dfrac{fk_{\text{d}}}{i\omega\mu_{\text{d}}}\dfrac{\gamma^{ze}_{n\text{N}}}{K_n(k_{\text{d}}R)}K'_n(k_{\text{d}}R)} e^{in(\phi-\phi')} \tag{94}$$

$$G^{r\phi}_{HH\text{d}}(r,\phi;R,\phi') = \frac{1}{2\pi}\sum_{n=-\infty}^{\infty} \frac{-nf}{\omega\mu_{\text{d}}}\frac{\gamma^{ze}_{n\text{N}}}{K_n(k_{\text{d}}R)} \frac{K_n(k_{\text{d}}r)}{\gamma_{n\text{N}} - \dfrac{fk_{\text{d}}}{i\omega\mu_{\text{d}}}\dfrac{\gamma^{ze}_{n\text{N}}}{K_n(k_{\text{d}}R)}K'_n(k_{\text{d}}R)} e^{in(\phi-\phi')} \tag{95}$$

These $r > R$ dyadic Green's function elements are completely new and not only contain the denominator correction term but also functional forms that assure that any fields constructed from them will decay properly outside the device.

INHOMOGENEOUS THREE-DIMENSIONAL DYADIC GREEN'S FUNCTION

Three dimensions tremendously changes the level of analysis required and in addition gives us the full complement of electromagnetic field components. There are now three electric field components and three magnetic field components. Because of the nature of the source vector function generating the Green's function, there will be twelve individual dyadic Green's function elements. Two infinite summations are employed in creating each element: the double-sided summation on the azimuthal index n, which we saw before, and the added singled-sided perpendicular summation. The azimuthal summation is retained as the inner summation, and the perpendicular summation added as the outer summation.

Three-Dimensional Inhomogeneous Hard Wall Case

The perpendicular summation is expected to be very small, requiring only a few terms for normally thin circulators. Only those devices prepared in a more bulk, large-scale, waveguide format will need extra terms. Clearly, circulator substrate thicknesses small compared to the wavelength in ferrite will use only one term, because only the lowest-order perpendicular mode will satisfy the bottom ground plane and upper microstrip shield boundary conditions. Referring to Krowne (8),

$$G^{z\phi}_{EHi} = \frac{1}{2\pi}\sum_{j=0}^{\infty}\sum_{n=-\infty}^{\infty} K_{zj+}\cos(k_{zij+}z)\frac{1}{D_{ABj}} \times [B^2_{nj}T^{z1}_{neji}(r) - B^1_{nj}T^{z2}_{neji}(r)]e^{-in\phi^q_k}e^{in\phi} \tag{96}$$

$$G^{zz}_{EHi} = \frac{1}{2\pi}\sum_{j=0}^{\infty}\sum_{n=-\infty}^{\infty} K_{zj+}\cos(k_{zij+}z)\frac{1}{D_{ABj}} \times [A^1_{nj}T^{z2}_{neji}(r) - A^2_{nj}T^{z1}_{neji}(r)]e^{-in\phi^q_k}e^{in\phi} \tag{97}$$

$$G^{\phi\phi}_{EHi} = \frac{1}{2\pi}\sum_{j=0}^{\infty}\sum_{n=-\infty}^{\infty} iK_{zj+}\sin(k_{zij+}z)\frac{1}{D_{ABj}} \times [B^2_{nj}T^{\phi1}_{neji}(r) - B^1_{nj}T^{\phi2}_{neji}(r)]e^{-in\phi^q_k}e^{in\phi} \tag{98}$$

$$G^{\phi z}_{EHi} = \frac{1}{2\pi}\sum_{j=0}^{\infty}\sum_{n=-\infty}^{\infty} iK_{zj+}\sin(k_{zij+}z)\frac{1}{D_{ABj}} \times [A^1_{nj}T^{\phi2}_{neji}(r) - A^2_{nj}T^{\phi1}_{neji}(r)]e^{-in\phi^q_k}e^{in\phi} \tag{99}$$

$$G^{r\phi}_{EHi} = \frac{1}{2\pi}\sum_{j=0}^{\infty}\sum_{n=-\infty}^{\infty} iK_{zj+}\sin(k_{zij+}z)\frac{1}{D_{ABj}} \times [B^2_{nj}T^{r1}_{neji}(r) - B^1_{nj}T^{r2}_{neji}(r)]e^{-in\phi^q_k}e^{in\phi} \tag{100}$$

$$G^{rz}_{EHi} = \frac{1}{2\pi}\sum_{j=0}^{\infty}\sum_{n=-\infty}^{\infty} iK_{zj+}\sin(k_{zij+}z)\frac{1}{D_{ABj}} \times [A^1_{nj}T^{r2}_{neji}(r) - A^2_{nj}T^{r1}_{neji}(r)]e^{-in\phi^q_k}e^{in\phi} \tag{101}$$

$$G^{z\phi}_{HHi} = \frac{1}{2\pi}\sum_{j=0}^{\infty}\sum_{n=-\infty}^{\infty} iK_{zj+}\sin(k_{zij+}z)\frac{1}{D_{ABj}} \times [B^2_{nj}T^{z1}_{nhji}(r) - B^1_{nj}T^{z2}_{nhji}(r)]e^{-in\phi^q_k}e^{in\phi} \tag{102}$$

$$G^{zz}_{HHi} = \frac{1}{2\pi}\sum_{j=0}^{\infty}\sum_{n=-\infty}^{\infty} iK_{zj+}\sin(k_{zij+}z)\frac{1}{D_{ABj}} \times [A^1_{nj}T^{z2}_{nhji}(r) - A^2_{nj}T^{z1}_{nhji}(r)]e^{-in\phi^q_k}e^{in\phi} \tag{103}$$

$$G^{\phi\phi}_{HHi} = \frac{1}{2\pi} \sum_{j=0}^{\infty} \sum_{n=-\infty}^{\infty} K_{zj+} \cos(k_{zij+}z) \frac{1}{D_{ABj}} \times [B^2_{nj} T^{\phi 1}_{nhji}(r) - B^1_{nj} T^{\phi 2}_{nhji}(r)] e^{-in\phi^q_k} e^{in\phi} \tag{104}$$

$$G^{\phi z}_{HHi} = \frac{1}{2\pi} \sum_{j=0}^{\infty} \sum_{n=-\infty}^{\infty} K_{zj+} \cos(k_{zij+}z) \frac{1}{D_{ABj}} \times [A^1_{nj} T^{\phi 2}_{nhji}(r) - A^2_{nj} T^{\phi 1}_{nhji}(r)] e^{-in\phi^q_k} e^{in\phi} \tag{105}$$

$$G^{r\phi}_{HHi} = \frac{1}{2\pi} \sum_{j=0}^{\infty} \sum_{n=-\infty}^{\infty} K_{zj+} \cos(k_{zij+}z) \frac{1}{D_{ABj}} \times [B^2_{nj} T^{r1}_{nhji}(r) - B^1_{nj} T^{r2}_{nhji}(r)] e^{-in\phi^q_k} e^{in\phi} \tag{106}$$

$$G^{rz}_{HHi} = \frac{1}{2\pi} \sum_{j=0}^{\infty} \sum_{n=-\infty}^{\infty} K_{zj+} \cos(k_{zij+}z) \frac{1}{D_{ABj}} \times [A^1_{nj} T^{r2}_{nhji}(r) - A^2_{nj} T^{r1}_{nhji}(r)] e^{-in\phi^q_k} e^{in\phi} \tag{107}$$

These expressions are quite a bit more involved than the 2-D dyadic Green's function formulas in Eqs. (56) to (58), with which the 3-D expressions in Eqs. (96), (104), and (106) are directly associated.

Three-Dimensional Inhomogeneous Soft Wall Case

The form of the dyadic Green's function elements for $r < R$ inside the ferrite puck is very similar to Eqs. (96) to (107) of the hard wall case, so they will not be provided here, but the elements for $r > R$ outside of the ferrite puck region will be given. Further information on the construction of these elements can be found in Krowne (9):

$$G^{z\phi}_{EH\mathrm{d}} = \frac{1}{2\pi} \sum_{j=0}^{\infty} \sum_{n=-\infty}^{\infty} f K^{\phi}_{zj} \cos(k_{zj}z) \frac{1}{D_{\overline{A}\overline{B}j}} ({}^{e}_{z}A^1_{nj} \overline{B}^2_{nj} - {}^{e}_{z}A^2_{nj} \overline{B}^1_{nj}) \frac{K_n(\sigma_{\mathrm{d}j} r)}{K_n(\sigma_{\mathrm{d}j} R)} e^{in(\phi-\phi')} \tag{108}$$

$$G^{zz}_{EH\mathrm{d}} = \frac{1}{2\pi} \sum_{j=0}^{\infty} \sum_{n=-\infty}^{\infty} f K^{z}_{zj} \cos(k_{zj}z) \frac{1}{D_{\overline{A}\overline{B}j}} ({}^{e}_{z}A^2_{nj} \overline{A}^1_{nj} - {}^{e}_{z}A^1_{nj} \overline{A}^2_{nj}) \frac{K_n(\sigma_{\mathrm{d}j} r)}{K_n(\sigma_{\mathrm{d}j} R)} e^{in(\phi-\phi')} \tag{109}$$

$$G^{r\phi}_{EH\mathrm{d}} = \frac{1}{2\pi} \sum_{j=1}^{\infty} \sum_{n=-\infty}^{\infty} i f K^{\phi}_{zj} \sin(k_{zj}z) \left(\frac{ins_j}{rD_{\overline{A}\overline{B}j}} ({}^{hd}_{z}A^1_{nj} \overline{B}^2_{nj} - {}^{hd}_{z}A^2_{nj} \overline{B}^1_{nj}) \frac{K'_n(\sigma_{\mathrm{d}j} r)}{K_n(\sigma_{\mathrm{d}j} R)} + \frac{inp_j}{rD_{\overline{A}\overline{B}j}} ({}^{e}_{z}A^1_{nj} \overline{B}^2_{nj} - {}^{e}_{z}A^2_{nj} \overline{B}^1_{nj}) \frac{K_n(\sigma_{dj} r)}{K_n(\sigma_{dj} R)} \right) e^{in(\phi-\phi')} \tag{110}$$

$$G^{rz}_{EH\mathrm{d}} = \frac{1}{2\pi} \sum_{j=1}^{\infty} \sum_{n=-\infty}^{\infty} i f K^{z}_{zj} \sin(k_{zj}z) \left(\frac{ins_j}{rD_{\overline{A}\overline{B}j}} ({}^{hd}_{z}A^2_{nj} \overline{A}^1_{nj} - {}^{hd}_{z}A^1_{nj} \overline{A}^2_{nj}) \frac{K'_n(\sigma_{\mathrm{d}j} r)}{K_n(\sigma_{\mathrm{d}j} R)} + \frac{p_j \sigma_{dj}}{D_{\overline{A}\overline{B}j}} ({}^{e}_{z}A^2_{nj} \overline{A}^1_{nj} - {}^{e}_{z}A^1_{nj} \overline{A}^2_{nj}) \frac{K_n(\sigma_{\mathrm{d}j} r)}{K_n(\sigma_{\mathrm{d}j} R)} \right) e^{in(\phi-\phi')} \tag{111}$$

$$G^{\phi\phi}_{EH\mathrm{d}} = \frac{1}{2\pi} \sum_{j=1}^{\infty} \sum_{n=-\infty}^{\infty} i f K^{\phi}_{zj} \sin(k_{zj}z) \left(\frac{-s_j}{D_{\overline{A}\overline{B}j}} ({}^{h\mathrm{d}}_{z}A^1_{nj} \overline{B}^2_{nj} - {}^{h\mathrm{d}}_{z}A^2_{nj} \overline{B}^1_{nj}) \frac{K'_n(\sigma_{\mathrm{d}j} r)}{K_n(\sigma_{\mathrm{d}j} R)} + \frac{inp_j \sigma_{dj}}{rD_{\overline{A}\overline{B}j}} ({}^{e}_{z}A^1_{nj} \overline{B}^2_{nj} - {}^{e}_{z}A^2_{nj} \overline{B}^1_{nj}) \frac{K_n(\sigma_{\mathrm{d}j} r)}{K_n(\sigma_{\mathrm{d}j} R)} \right) e^{in(\phi-\phi')} \tag{112}$$

$$G^{\phi z}_{EH\mathrm{d}} = \frac{1}{2\pi} \sum_{j=1}^{\infty} \sum_{n=-\infty}^{\infty} i f K^{z}_{zj} \sin(k_{zj}z) \left(\frac{-s_j \sigma_{dj}}{D_{\overline{A}\overline{B}j}} ({}^{h\mathrm{d}}_{z}A^2_{nj} \overline{A}^1_{nj} - {}^{h\mathrm{d}}_{z}A^1_{nj} \overline{A}^2_{nj}) \frac{K'_n(\sigma_{dj} r)}{K_n(\sigma_{dj} R)} + \frac{inp_j}{rD_{\overline{A}\overline{B}j}} ({}^{e}_{z}A^2_{nj} \overline{A}^1_{nj} - {}^{e}_{z}A^1_{nj} \overline{A}^2_{nj}) \frac{K_n(\sigma_{dj} r)}{K_n(\sigma_{dj} R)} \right) e^{in(\phi-\phi')} \tag{113}$$

$$G^{z\phi}_{HH\mathrm{d}} = \frac{1}{2\pi} \sum_{j=1}^{\infty} \sum_{n=-\infty}^{\infty} i f K^{\phi}_{zj} \sin(k_{zj}z) \frac{1}{D_{\overline{A}\overline{B}j}} ({}^{h\mathrm{d}}_{z}A^1_{nj} \overline{B}^2_{nj} - {}^{h\mathrm{d}}_{z}A^2_{nj} \overline{B}^1_{nj}) \frac{K_n(\sigma_{\mathrm{d}j} r)}{K_n(\sigma_{\mathrm{d}j} R)} e^{in(\phi-\phi')} \tag{114}$$

$$G^{zz}_{HH\mathrm{d}} = \frac{1}{2\pi} \sum_{j=1}^{\infty} \sum_{n=-\infty}^{\infty} i f K^{z}_{zj} \sin(k_{zj}z) \frac{1}{D_{\overline{A}\overline{B}j}} ({}^{h\mathrm{d}}_{z}A^2_{nj} \overline{A}^1_{nj} - {}^{h\mathrm{d}}_{z}A^1_{nj} \overline{A}^2_{nj}) \frac{K_n(\sigma_{\mathrm{d}j} r)}{K_n(\sigma_{\mathrm{d}j} R)} e^{in(\phi-\phi')} \tag{115}$$

$$G^{\phi\phi}_{HH\mathrm{d}} = \frac{1}{2\pi} \sum_{j=0}^{\infty} \sum_{n=-\infty}^{\infty} f K^{\phi}_{zj} \cos(k_{zj}z) \frac{1}{D_{\overline{A}\overline{B}j}} ({}^{h\mathrm{d}}_{\phi}A^1_{nj}(r) \overline{B}^2_{nj} - {}^{h\mathrm{d}}_{\phi}A^2_{nj}(r) \overline{B}^1_{nj}) e^{in(\phi-\phi')} \tag{116}$$

$$G^{\phi z}_{HH\mathrm{d}} = \frac{1}{2\pi} \sum_{j=0}^{\infty} \sum_{n=-\infty}^{\infty} f K^{z}_{zj} \cos(k_{zj}z) \frac{1}{D_{\overline{A}\overline{B}j}} ({}^{h\mathrm{d}}_{\phi}A^1_{nj}(r) \overline{A}^2_{nj} - {}^{h\mathrm{d}}_{\phi}A^2_{nj}(r) \overline{A}^1_{nj}) e^{in(\phi-\phi')} \tag{117}$$

$$G^{r\phi}_{HH\mathrm{d}} = \frac{1}{2\pi} \sum_{j=1}^{\infty} \sum_{n=-\infty}^{\infty} i f K^{\phi}_{zj} \sin(k_{zj}z) \left(\frac{p_j \sigma_{\mathrm{d}j}}{D_{\overline{A}\overline{B}j}} ({}^{h\mathrm{d}}_{z}A^1_{nj} \overline{B}^2_{nj} - {}^{h\mathrm{d}}_{z}A^2_{nj} \overline{B}^1_{nj}) \frac{K'_n(\sigma_{\mathrm{d}j} r)}{K_n(\sigma_{\mathrm{d}j} R)} + \frac{inu_j}{rD_{\overline{A}\overline{B}j}} ({}^{e}_{z}A^1_{nj} \overline{B}^2_{nj} - {}^{e}_{z}A^2_{nj} \overline{B}^1_{nj}) \frac{K_n(\sigma_{\mathrm{d}j} r)}{K_n(\sigma_{\mathrm{d}j} R)} \right) e^{in(\phi-\phi')} \tag{118}$$

$$G^{rz}_{HH\mathrm{d}} = \frac{1}{2\pi} \sum_{j=1}^{\infty} \sum_{n=-\infty}^{\infty} i f K^{z}_{zj} \sin(k_{zj}z) \left(\frac{p_j \sigma_{\mathrm{d}j}}{D_{\overline{A}\overline{B}j}} ({}^{h\mathrm{d}}_{z}A^2_{nj} \overline{A}^1_{nj} - {}^{h\mathrm{d}}_{z}A^1_{nj} \overline{A}^2_{nj}) \frac{K'_n(\sigma_{\mathrm{d}j} r)}{K_n(\sigma_{\mathrm{d}j} R)} + \frac{inu_j}{rD_{\overline{A}\overline{B}j}} ({}^{e}_{z}A^2_{nj} \overline{A}^1_{nj} - {}^{e}_{z}A^1_{nj} \overline{A}^2_{nj}) \frac{K_n(\sigma_{dj} r)}{K_n(\sigma_{dj} R)} \right) e^{in(\phi-\phi')} \tag{119}$$

The 3-D dyadic Green's function formulas in Eqs. (108), (116), and (118) are directly associated with the 2-D expressions in Eqs. (59) to (61), which are much simpler.

MULTIPLE LAYERS UNDER THE CIRCULATOR METALLIZATION

Circulator structures realized in the laboratory and in industrial applications are made either with a single substrate or with several layers. The single substrate case obviously occurs when the substrate and the ferrite material are one and the same. But due to complications of mechanical and material processing steps, several layers may exist. The designer can expect layers that do not exhibit nonreciprocal action to reduce the effectiveness of the finished circulator device when this layered effect shows up in the region under the shield. Structures that use pucks dropped into an existing substrate, whether of dielectric or of other ferrite material, will not suffer degradation in the main spatial operating region of the device. Film processes, which rely on deposition on top of an existing semiconductor semiinsulating substrate, or on top of an insulator, will produce the layered effect under the shield. It is possible to avoid this effect if the metal ground plane for the device can be deposited on top of the substrate, thereby bringing up the ground plane from below, and then depositing the ferrite film.

Assuming that we have a layered situation and would like to amend the 2-D Green's function solver to model the device, a first-order method, originally proposed by Neidert (10), is available to estimate the new tensor permeability and permittivity. [Discussion about how to develop a self-consistent rigorous approach based on three dimensions is found in Krowne (8).] For a two-layered medium consisting of the ferrite and a dielectric, for example, an equivalent medium is found that is uniform, and this then is consistent with the 2-D nature of the problem, which is collapsed in the third dimension. Equivalent distributed capacitance or inductance of a mixed insulator transmission line and equivalent series inductance of a transmission line with lossy magnetic conductors are employed. Electric equivalence is established by using an equivalent permittivity that makes the shunt capacitance of the equivalent material equal to that of the real layered medium. Magnetic equivalence is established by using an equivalent permeability that makes the series inductance of the equivalent material equal to that of the real layered medium.

Applying Gauss's and Ampere's laws, the derived relationships for the equivalent RF permittivity ϵ_{eq} and equivalent RF permeability tensor $\overleftrightarrow{\mu}_{\mathrm{eq}}$ are

$$\epsilon_{\mathrm{eq}} = \frac{\epsilon_{\mathrm{d}}\epsilon_{\mathrm{f}}}{\epsilon_{\mathrm{d}}\dfrac{d_{\mathrm{f}}}{d} + \epsilon_{\mathrm{f}}\dfrac{d_{\mathrm{d}}}{d}} \tag{120}$$

$$\overleftrightarrow{\mu}_{\mathrm{eq}} = \overleftrightarrow{\mu}_{\mathrm{d}}\frac{d_{\mathrm{d}}}{d} + \overleftrightarrow{\mu}_{\mathrm{f}}\frac{d_{\mathrm{f}}}{d} \tag{121}$$

In Eq. (120), ϵ_{d} and ϵ_{f} are respectively the dielectric and ferrite permittivities. The total substrate thickness d is merely

$$d = d_{\mathrm{d}} + d_{\mathrm{f}} \tag{122}$$

Equation (121) arises from Eq. (1) on using the Polder tensor expressions for complex μ and κ, and adding the subscript f to the tensor permeability to be absolutely unambiguous. The dielectric permeability, a scalar (and assumed for simplicity to be unity times the free space value), is upgraded to an identity tensor,

$$\overleftrightarrow{\mu}_{\mathrm{d}} = \mu_0 \overleftrightarrow{\boldsymbol{I}} \tag{123}$$

Inserting Eqs. (1) and (122) into Eq. (121) gives the new equivalent single-medium permeability tensor:

$$\overleftrightarrow{\mu}_{\mathrm{eq}} = \mu_0 \begin{bmatrix} \dfrac{d_{\mathrm{d}}}{d} + \mu\dfrac{d_{\mathrm{d}}}{d} & -j\kappa\dfrac{d_{\mathrm{f}}}{d} & 0 \\ j\kappa\dfrac{d_{\mathrm{f}}}{d} & \dfrac{d_{\mathrm{d}}}{d} + \mu\dfrac{d_{\mathrm{d}}}{d} & 0 \\ 0 & 0 & 1 \end{bmatrix} \tag{124}$$

LOSS CONTRIBUTIONS

Metallic, dielectric, and magnetic losses are the basic loss mechanisms to be dealt with in circulator devices. When ferrite materials are utilized with low intrinsic losses, then metallic losses of the conductors constituting the circulator structure will dominate, this being especially true for thin substrates. A uniform Green's function solver by Neidert and Philips (11) has been utilized to calculate dissipation losses versus substrate thickness for a C-band (6 GHz) YIG circulator. The insertion loss versus substrate thickness for a YIG film on silicon substrate higher frequency X-band (10 GHz) device has been calculated by Adam et al. (12) using the uniform Green's function method due to Neidert and Philips (11). The lossless Green's function code was modified by an ad hoc, heuristic approach to allow for losses, and to its credit, it can be said to predict circulator losses reasonably well, having been verified by numerous experimental s-parameter measurements. Green's function code for inhomogeneous circulators has also been modified along the same lines by Neidert (10), keeping intact the basic inhomogeneous recursive Green's function construction developed by Krowne (6).

A rigorous first-order method has been derived recently by Krowne (13) for treating metallic loss of the circulator. It assumes that the film thickness is small compared to a wavelength, the electromagnetic problem is basically 2-D, and a small patch under the shield with a circulating curved azimuthal wave can be used to characterize the whole patch by a scaling procedure based on total area. The theory becomes essentially that of a parallel plate waveguiding situation.

The effective permeability within the ferrite region, assuming an $e^{j\omega t}$ time dependence, from this theory is

$$\begin{aligned} \mu_{\mathrm{eq}} &= \frac{\mu_{\mathrm{f}}}{\left(1 - (1-j)\dfrac{\delta}{d}\dfrac{\mu_{\mathrm{m}}}{\mu_{\mathrm{f}}}\right)^2} \\ &\approx \mu_{\mathrm{f}}\left(1 + 2(1-j)\frac{\delta}{d}\frac{\mu_{\mathrm{m}}}{\mu_{\mathrm{f}}}\right) \end{aligned} \tag{125}$$

Equation (125) provides an equivalent permeability for the ferrite region, which accounts for the whole circulator structure under the shield, the imperfect metal regions and the main ferrite puck region. The second approximation in the equation is true for small corrections, implicit in the whole derivation. What is placed in the formulas in Eq. (125) for μ_{f}

is the 2-D effective permeability for the ferrite. The ratio of skin depth to substrate thickness is δ/d, and μ_m/μ_f is the metal-to-ferrite permeability ratio.

The last thing to do is to obtain an effective propagation constant in the ferrite medium. It is found by invoking the first equality in Eq. (125):

$$k_{\mathrm{eq,p}} = k_{\mathrm{eq,f}} = \omega\sqrt{\epsilon_{\mathrm{f}}\mu_{\mathrm{eq,f}}} = \omega\sqrt{\epsilon_{\mathrm{f}}\mu_{\mathrm{f}}}\,\frac{1}{1-(1-j)(\delta/d)/(\mu_{\mathrm{m}}/\mu_{\mathrm{f}})}$$
$$= k_{\mathrm{f}}\frac{1}{1-(1-j)(\delta/d)/(\mu_{\mathrm{m}}/\mu_{\mathrm{f}})} \approx k_{\mathrm{f}}\left(1+(1-j)\frac{\delta}{d}\frac{\mu_{\mathrm{m}}}{\mu_{\mathrm{f}}}\right) \tag{126}$$

MATCHING SECTIONS

Self-consistent electromagnetic solvers work on the premise that specific driving conditions exist at each circulator port, thereby exciting the internal fields of the device, sometimes referred to as the intrinsic device. This is true whether the solver is a Green's function method relying upon Dirac delta function sources at the port locations, or a finite-element method relying upon imposed fields at the port locations. In either case, the tangential $\boldsymbol{E}$ and $\boldsymbol{H}$ fields at the port locations on the circulator device perimeter $r = R$ must obey continuity with the tangential $\boldsymbol{E}$ and $\boldsymbol{H}$ fields in the exiting port transmission lines. These microstrip transmission lines have impedance Z_k for the kth port location, and their impedances are found by using the width determined from the extent of each particular port and the common substrate thickness. For ports of identical angular extent, all Z_k will be the same (making $Z_k = Z_0$, $k = 1, 2, \ldots, N$). The s parameters of the intrinsic circulator are referenced to these impedances, or impedance if they are all the same.

To facilitate the incorporation of the circulator device into a CAD program generating s parameters, the N-port device should be rereferenced to the system impedances Z'_k in use. Z'_k, $k = 1, 2, \ldots, N$, will usually be 50 Ω for microstrip circulators. Figure 3 shows a circuit sketch of a symmetrically disposed three-port device, where at progressively increasing radial distance from the central circulator puck, the s-parameter matrix goes from its intrinsic $N \times N$ value $\boldsymbol{S}_{\mathrm{in}} = \boldsymbol{S}_1$ to its rereferenced $N \times N$ value $\boldsymbol{S}_{\mathrm{re}} = \boldsymbol{S}_2$ to its final $N \times N$ value $\boldsymbol{S}_{\mathrm{m}} = \boldsymbol{S}$ after encountering a matching section with a 2×2 transfer matrix $\boldsymbol{T}_{\mathrm{M}}$. This last matrix will generally be referenced to the system matrix impedance Z_0.

Matching circuits for microstrip circulators are most commonly cascaded sections of transformers, usually quarter-wavelength sections, placed in the same configuration at each port. Computer codes have been developed by Krowne and Neidert (14,15) that incorporate such cascaded transformers directly into the s-parameter calculation. Each microstrip transformer section is permitted to have a user-chosen length and width. Dissipation losses are included in each microstrip transformer section, so that the final s parameters calculated include all intrinsic as well as extrinsic device losses. This is important for wide-bandwidth circulators having many quarter-wavelength matching sections, because the matching section losses frequently are greater than the intrinsic device losses. The final matched s parameters for the circulator structure are found by mapping or transforming $\boldsymbol{S}_2$ through $\boldsymbol{T}_{\mathrm{M}}$, yielding $\boldsymbol{S}$.

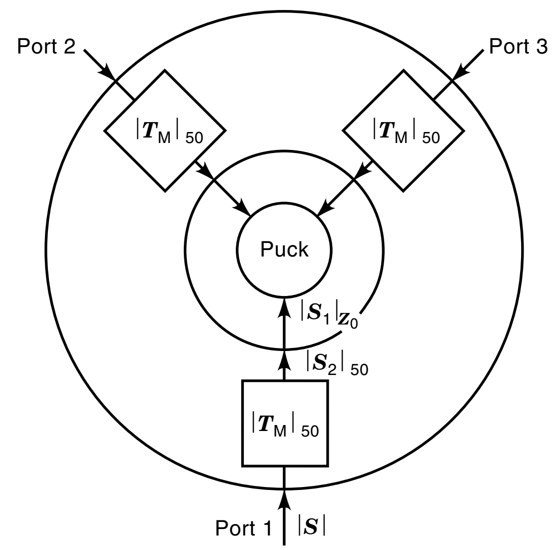

Figure 3. Intrinsic circulator (shown as a puck) and its matching circuit network consisting of transformer sections.

NUMERICAL STUDIES AND COMPARISON WITH EXPERIMENT

Circulator performance requires that the s parameters of the device be found. These parameters, which relate to voltage wave ratios, can be determined once the Green's function solutions have be secured. The Green's functions are used to find the s parameters under source and boundary condition constraints, besides using the definitions of the s parameters. The field distribution within the circulator puck can also be examined once the Green's function solutions become available. Very informative contour diagrams of electric and magnetic fields may be found, which provide insight on how the circulator performs its nonreciprocal operation.

Electromagnetic Fields and *S* Parameters

Consider characterizing each individual port by a single segment, and choose three ports to interface with the outside circuit for a 2-D Green's function model. Then the expression for the electric field within the circulator puck, approximating the contour integral along the perimeter at each port by a discrete sum (of one element here), is

$$E_z(r,\phi) = \sum_{q=1}^{N_{\mathrm{T}}^{\mathrm{d}}} G_{EH}^{z\phi}(r,\phi;R,\phi^{\mathrm{q}})H_{\phi\mathrm{c}}(R,\phi^{\mathrm{q}})\,\Delta\phi^{\mathrm{q}} \tag{127}$$

where $N_{\mathrm{T}}^{\mathrm{d}} = 3$, and $H_{\phi\mathrm{c}}(R, \phi)$ are the magnetic field sources driving the device. Equation (127) gives the electric field anywhere within the puck. Sources $H_{\phi\mathrm{c}}(R, \phi)$ at the perimeter of the device may be found self-consistently with the internal electromagnetic behavior of the puck and the external circuit network by using the loading conditions

$$\frac{E^{\mathrm{a}}_{z(\mathrm{in})}}{H_{\mathrm{a(in)}}} = \zeta_{\mathrm{a}} \tag{128}$$

$$\frac{E^{\mathrm{b}}_{z(\mathrm{out})}}{H_{\mathrm{b(out)}}} = -\zeta_{\mathrm{b}} \tag{129}$$

$$\frac{E^{\mathrm{c}}_{z(\mathrm{out})}}{H_{\mathrm{c(out)}}} = -\zeta_{\mathrm{c}} \tag{130}$$

The internal electromagnetic behavior within the puck is evaluated at the circulator perimeter by setting $r = R$ in Eq. (127). Next we absorb the azimuthal spread of each port into the Green's function by defining a streamlined dyadic Green's function element

$$G(\phi, \phi_{\mathrm{q}}) = G^{z\phi}_{EH}(R, \phi; R, \phi_{\mathrm{q}})\,\Delta\phi_{\mathrm{q}} \tag{131}$$

where the understood indices and arguments have been dropped. The convenient form in Eq. (131) is now used to expand Eq. (127) at the perimeter:

$$E_z(R, \phi) = G(\phi, \phi_{\mathrm{a}})H_{\phi\mathrm{a}} + G(\phi, \phi_{\mathrm{b}})H_{\phi\mathrm{b}} + G(\phi, \phi_{\mathrm{c}})H_{\phi\mathrm{c}} \tag{132}$$

Now evaluate Eq. (132) at each of the ports, q = a, b, c, labeled counterclockwise, and simplify the notation for $E_z(R, \phi)$ to E^q_z by setting $\phi = \phi_q$:

$$E^{\mathrm{a}}_z = G(\phi_{\mathrm{a}}, \phi_{\mathrm{a}})H_{\phi\mathrm{a}} + G(\phi_{\mathrm{a}}, \phi_{\mathrm{b}})H_{\phi\mathrm{b}} + G(\phi_{\mathrm{a}}, \phi_{\mathrm{c}})H_{\phi\mathrm{c}} \tag{133}$$

$$E^{\mathrm{b}}_z = G(\phi_{\mathrm{b}}, \phi_{\mathrm{a}})H_{\phi\mathrm{a}} + G(\phi_{\mathrm{b}}, \phi_{\mathrm{b}})H_{\phi\mathrm{b}} + G(\phi_{\mathrm{b}}, \phi_{\mathrm{c}})H_{\phi\mathrm{c}} \tag{134}$$

$$E^{\mathrm{c}}_z = G(\phi_{\mathrm{c}}, \phi_{\mathrm{a}})H_{\phi\mathrm{a}} + G(\phi_{\mathrm{c}}, \phi_{\mathrm{b}})H_{\phi\mathrm{b}} + G(\phi_{\mathrm{c}}, \phi_{\mathrm{c}})H_{\phi\mathrm{c}} \tag{135}$$

Once the $H_{\phi i}$ fields (i = a, b, c) have been found from Eqs. (128) to (130) and (133) to (135), the s parameters can be obtained from

$$s_{11} = 1 - \zeta_{\mathrm{a}}H_{\mathrm{a}} \tag{136}$$

$$s_{21} = E^{\mathrm{b}}_z = -\zeta_{\mathrm{b}}H_{\mathrm{b}} \tag{137}$$

$$s_{31} = E^{\mathrm{c}}_z = -\zeta_{\mathrm{c}}H_{\mathrm{c}} \tag{138}$$

Equation (127) provides the recipe for computing the electric field distribution within the circulator puck. The two magnetic field components H_r, H_ϕ may also be sought from dyadic Green's function expansions similar to Eq. (127).

Circulator Performance and Field Contour Plots

The circulator port impedances (looking into the device) are generally quite a bit lower than the standard 50 Ω reference impedance system. Because of this problem, actual circulator devices prepared in industry for insertion into circuits need transition networks between the circulator puck perimeter and the final circuit to be matched. Figure 4 and the previous discussion indicate how this matching process is accomplished. Figure 4 shows a top view of what the metallization should look like. Calculations reported here use the one-stage transformer section shown in the figure. Figure 5 gives a realistic variation of the demagnetizing factor N_{zz} expected in an actual device. It is fairly constant (80% to 90%) until the edge of the puck is approached (within 70% of the edge in terms of the total radius); then the value dives to 45%. It is this very nonlinear change in N_{zz} that makes the partitioning of the puck necessary and the recursive dyadic Green's function invaluable for correct modeling of the circulator. The applied magnetic bias field, a static field, is not always constant. Instead, the field seen by the circulator is dependent upon the

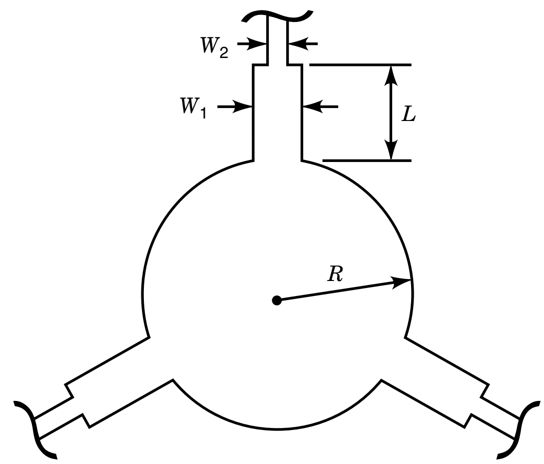

Figure 4. Top view of the a circulator metallization pattern used in actual calculations for a nominal 8 GHz X-band device. Outside the puck shield are three identical quarter-wave transformers, which transition to narrower microstrip lines. The substrate is Trans-Tech G113, $4\pi M_s$ = 1780 G, ΔH = 45 Oe, ϵ_r = 15.0, tan δ = 0.0002, substrate thickness = 0.051 cm, and conductor thickness = 0.0005 cm. R = 0.279 w_1 = 0.096 cm, w_2 = 0.030 cm (50 Ω transmission line), and L = 0.241 cm.

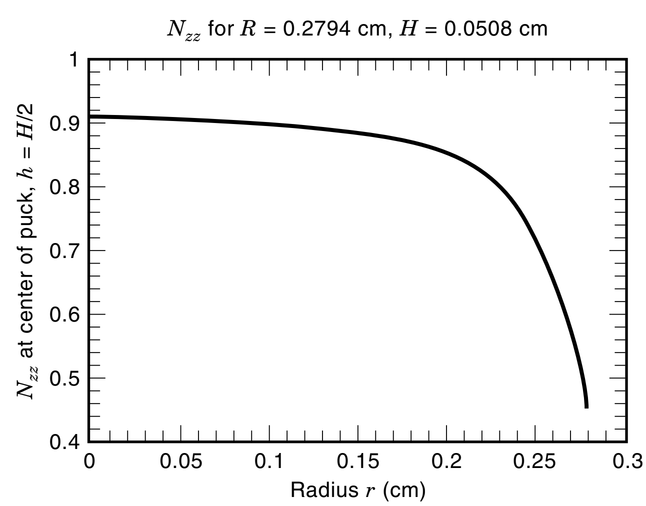

Figure 5. Example of the variation of the demagnetization factor N_{zz} with radial distance from the puck center for an X-band device.

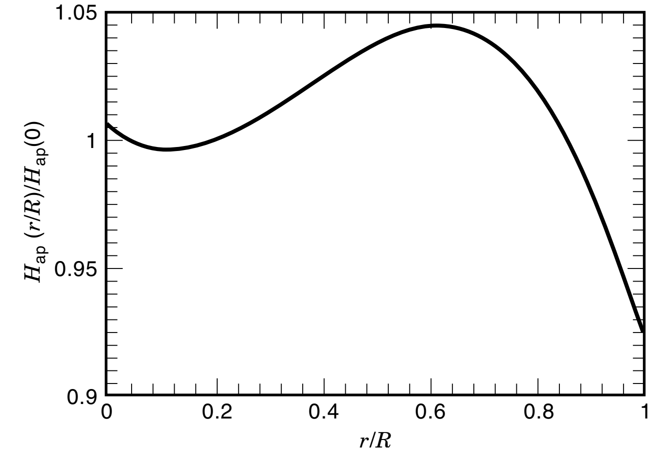

Figure 6. Example of the variation of the applied external bias field H_{app} with radial distance from the puck center for an X-band device.

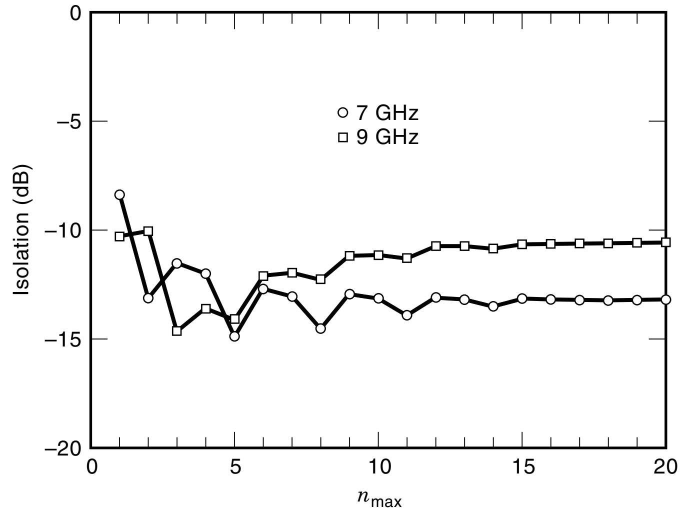

Figure 8. Convergence behavior of isolation versus n_{max} at two frequencies, 7 GHz and 9 GHz, selected from a diagram such as in Fig. 7, but for a uniform case. A single quarter-wavelength transformer is utilized in the matching network at each port. Results are given in a 50 Ω reference system.

precise magnet location and the attendant magnetic circuitry. The shape of H_{ap} might look like that seen in Fig. 6.

Numerical robustness depends upon the convergence behavior of the solution and the computation time to determine the solution. Figure 7 provides a plot, for an inhomogeneous circulator, of the isolation s_{31} against frequency for six truncated cases of the doubled-sided infinite azimuthal summations used in the dyadic Green's function evaluations. The maximum azimuthal index used is denoted by n_{max}, and we show n_{max} = 3, 6, 9, 18, 36, 72 for the X-band device. n_{max} must be at least 18 before the solution is within ±0.25 dB of the final value. For a uniform device n_{max} may be chosen smaller to obtain similar accuracy. For example, $n_{max} = 9$ yields convergence to within ±0.40 dB of the final value for the uniform device.

Figure 7 gives an overall idea of what happens over the entire circulator bandwidth, but fails to provide detailed information on convergence under unity incremental variation of n_{max}. This is given for a uniform device in Figs. 8 and 9, which show the results at two selected microwave frequencies for, respectively, a matched circulator and an intrinsic (or bare) circulator. The two frequencies straddle the 8 GHz center frequency. Clearly, in comparing Figs. 8 and 9, we see that the introduction of matching transformers causes significant numerical oscillation to occur. This is not entirely unexpected, considering the manner in which a transformer operates. Convergence behavior with respect to the number of computational regions, N_R, which is equal to the number of annuli, N, plus one ($N_R = N + 1$), is shown in Fig. 10 for N_R = 1, 6, 16, 50. For N_R = 6 or greater, the numerically determined answer is accurate to within ±0.1 dB of the final value.

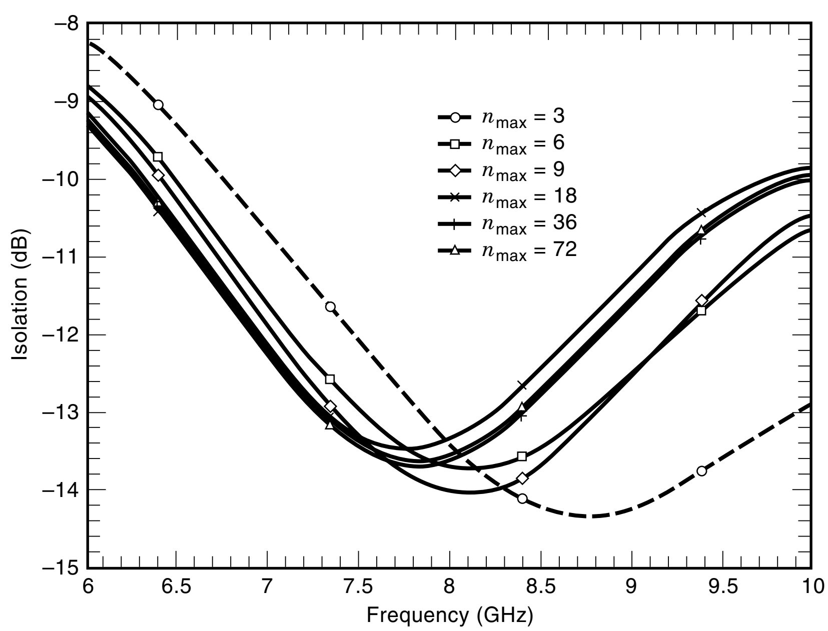

Figure 7. Isolation s_{31} versus frequency, with the curves parametrized in terms of n_{max}, the maximum azimuthal index number. A single ferrite material is used for the circulator puck, with a five-region model (one central disk plus four annuli) employed to represent the demagnetizing factor N_{zz}.

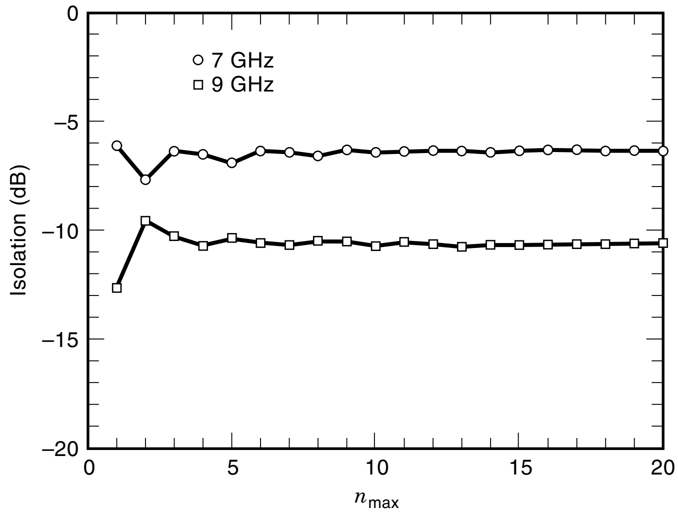

Figure 9. Convergence behavior of isolation versus n_{max} at two frequencies, 7 GHz and 9 GHz, selected from a diagram such as in Fig. 7, but for a uniform case. No transformer is utilized (only a central ferrite disk is present). Results are given in a 50 Ω reference system.

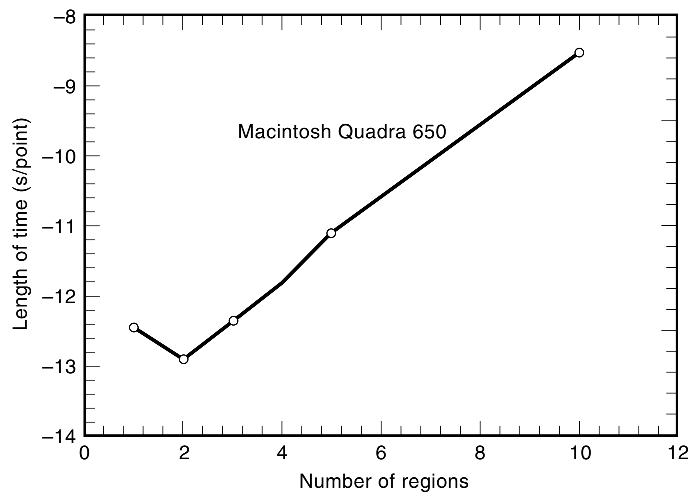

Figure 11. Computation time for a recursive Green's function calculation on a nominal 8 GHz circulator versus the number of regions, N_R. The inner disk is counted as the first region, with outlying annuli added afterward.

The particular dyadic Green's function types covered in this presentation can be evaluated extremely efficiently using FORTRAN computer codes. That this is so becomes apparent when studying Fig. 11, which plots computation time in seconds per frequency point against the number of regions, N_R. Run times are for execution on a Macintosh Quadra 650. The cost in time of using more regions increases nearly linearly at and beyond $N_R = 2$. The algorithmic difference for $N_R = 1$ has caused the initial decrease before the general trend becomes evident.

Use of the 2-D recursive Green's function computer code for the inhomogeneous situation allows comparison in Fig. 12 of measured and calculated (a) insertion loss s_{21} and return loss s_{11} and (b) isolation s_{31} versus frequency. It is seen that the calculated and measured insertion loss for the X-band circulator are in excellent agreement. Good agreement also exists for calculated and measured return loss, with a slight discrepancy between the minimum points. Acceptable agreement is found for calculated and measured isolation results, with the calculated results somewhat more favorable than actually seen in the lab. At the minimum point, the calculated value is 9 dB better. Imperfections in the fabricated device may account for much of the deviation seen between numerical calculation and experiment in Fig. 12. The onset of the next puck resonance causes the obvious glitches in the experimental curves between 12 GHz and 13 GHz at the high end of the operating band. Careful examination of the calculated curves shows evidence of this next resonance (small inflections, rises, and dips). The significant difference seen here between theory and experiment is most likely due to the large measured ferromagnetic linewidth $\Delta H = 320$ Oe assigned to the ferrite material used to fabricate the circulator. Reduction of ΔH makes the calculated and experimental results very similar. Direct visual evidence of this next resonance is provided in field patterns to be discussed shortly in Fig. 14.

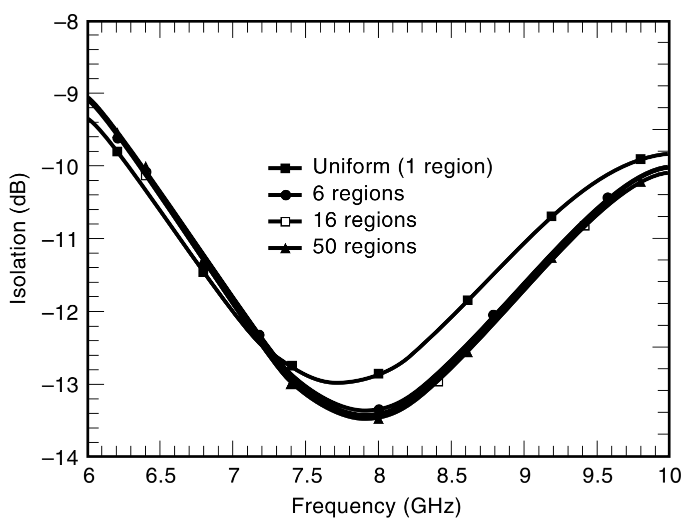

Figure 10. Isolation s_{31} versus frequency with the curves parametrized in terms of the number of regions N_R (= $N + 1$) used to model the demagnetizing factor N_{zz}.

Figures 13(a–c) show electric field patterns for the intrinsic inhomogeneous circulator (without any matching structures), calculated by the 2-D recursive Green's function computer code using an incident signal at each of the three ports with no incoming signal at the remaining two ports. When embedding the intrinsic device in a matching network, the actual electric field pattern obtained is shown in Fig. 13(d). Port loads attached to the circulator at each port are shown in Fig. 13(e). Each load consists of a quarter-wave matching network section and the system impedance. A null in the electric field pattern (lightest oval region) occurs in the first three panels of Fig. 13(a–c), but these nulls are not at the perimeter. They appear inside the puck for each port excitation case. Only in the matched device, which is excited essentially like (a), do we see a movement of the null to the perimeter, where it creates the very low desired isolation seen in the laboratory. The null gets partially absorbed, and widened on the perimeter of the circulator.

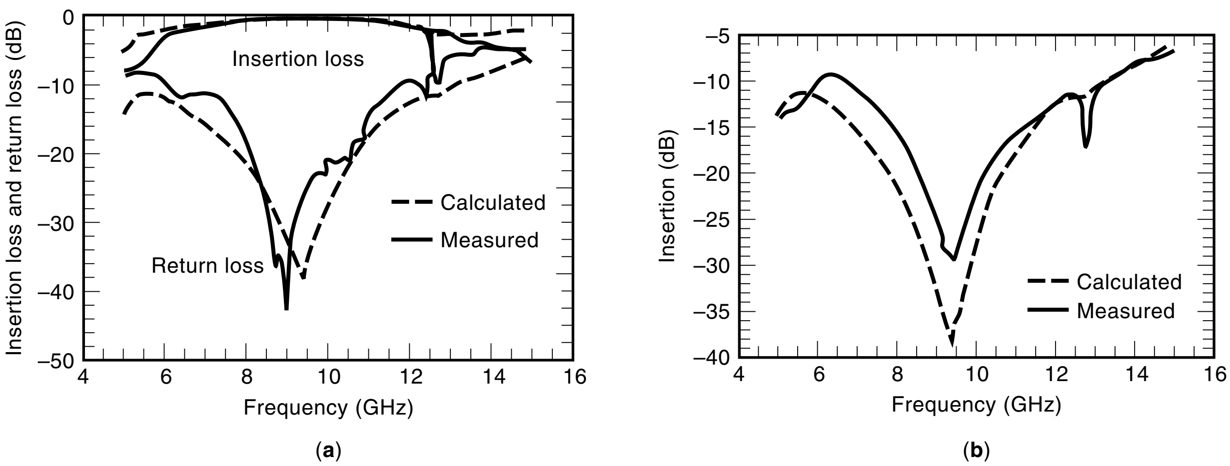

Figure 12. Measured and calculated (a) insertion loss s_{21} and return loss s_{11} and (b) isolation s_{31} versus frequency, using recursive Green's function computer code. $4\pi M_s = 2300$ G, $H_{ap} = 2300$ Oe, $\Delta H = 320$ Oe, $h = 0.635$ mm, $R = 2.7026$ mm, $w = 1.6561$ mm, $w_c = 1.4w$, $\epsilon_f = 13.3$, $\epsilon_d = 9.5$, tan $\delta = 0.0003$, and center frequency $f = 9.5$ GHz. (Device fabricated at EMS Technologies, Inc. by David Popelka and Gordon Harrison.)

A comment about the way the plots were constructed in Fig. 13 (and the following Fig. 14) is appropriate here. The interface between neighboring uniformly shaded regions represents a contour line of constant electric field magnitude. The first such line, encircling the lightest region, corresponds to 5% of the maximum value attained within the puck. We have referred to the lightest region as the "null" because it has field magnitudes below this tiny value, and inside its contour toward its center the values approach zero. Successive contours encircling ever larger regions or moving further away from the null correspond to 15%, 25%, 35%, 45%, 55%, 65%, 75%, 85%, and 95% of the maximum electric field value. Increasing darkness denotes increasing magnitude of the electric field. For example, the uniformly shaded region between the 35% and 45% contours must have $0.35|E_{z,\max}| \leq |E_z| \leq 0.45|E_{z,\max}|$.

The electric field pattern variation with frequency from 5 GHz to 13 GHz was calculated by using the 2-D recursive Green's function computer code and is shown in Fig. 14. Clockwise movement of the null, getting closer to the device perimeter, is seen before the center frequency (about 9 GHz) is attained. Once the center frequency is passed, the null pulls away from the perimeter, shrinks in size, and spawns a second null, both located within the puck.

FUTURE DEVELOPMENTS

There are other important and interesting subjects we have not been able to touch upon in this short summary. For example, symmetry considerations shown in Krowne (16) enable various Green's functions to be related to one another, reduc-

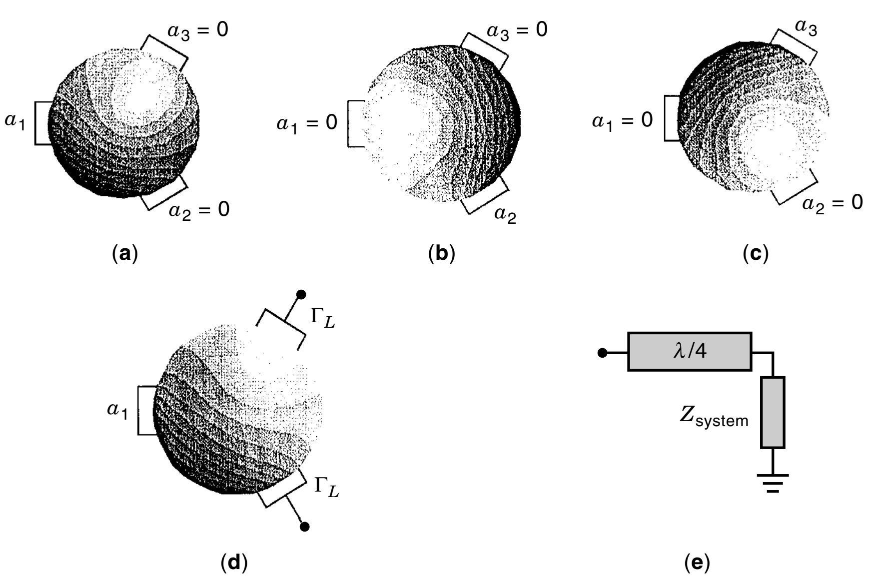

Figure 13. Electric field patterns for the intrinsic circulator (without any matching structures) as calculated by the 2-D recursive Green's function computer code using an incident signal at (a) port 1, (b) port 2, and (c) port 3, with no incoming signal at the remaining two ports for each case. (d) Electric field pattern obtained by immersing the intrinsic device in a matching network, consisting of individual port loads shown in (e). Shading indicates electric field magnitude, with the darkest region having the highest magnitude.

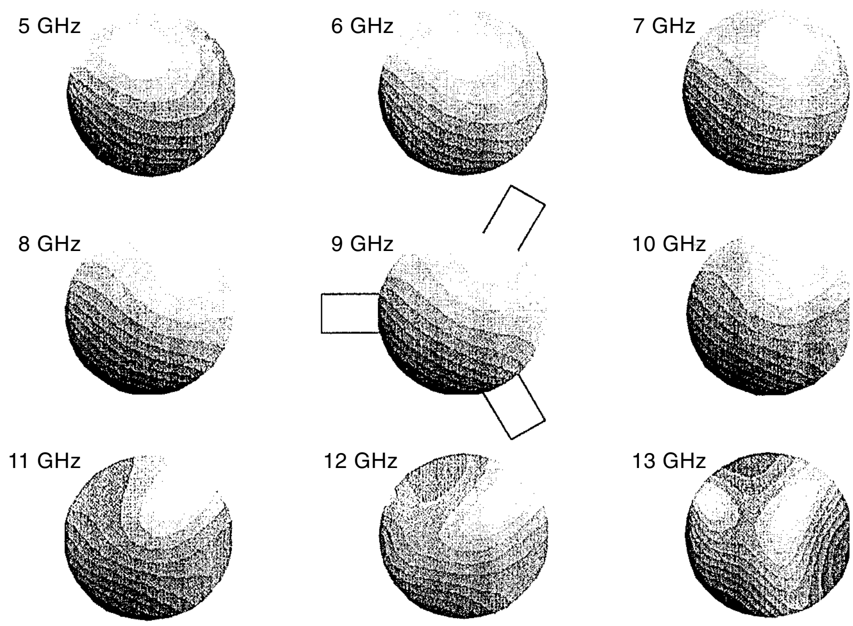

Figure 14. Electric field patterns for the intrinsic circulator embedded in a matching network are calculated by the 2-D recursive Green's function computer code, and displayed at nine individual frequencies. Shading indicates electric field magnitude, with the darkest region being the highest magnitude.

ing the mathematical load and in many cases cutting down on the number of Green's functions that must be evaluated to determine the *s* parameters (perimeter dyadic Green's functions) and the electromagnetic fields (internal and external dyadic Green's functions). For more realistic but complex geometries that include outlying substrate material and overlaying superstrate material, necessitating 3-D treatment, implicit dyadic Green's functions can be found in Krowne (17,18). These new implicit dyadic Green's functions have some of the properties, at least in terms of construction, of the explicit dyadic Green's functions, but with the new capability of handling external radial annular layers and external vertical layers. Use of compact matrix methods applied to the recursion process is described in Krowne (19) for the 2-D model. Such matrix techniques are very useful in the derivation of field expressions and in the development of efficient computer codes. Finally, information on design considerations for microwave frequencies is in Webb (20), and for millimeter-wave frequencies in Webb (20) and in Newman et al. (21).

Circulators are pivotal components in electronic equipment, and their use in potentially huge quantities in automotive and train distance ranging units, as well as other commercial ventures, may herald a promising future beyond what seems to be developing for military applications. CAD will play a critical role in these applications by allowing circulators to be rapidly designed to suit various requirements. Numerical modeling of circulators using efficient techniques, including rapidly convergent dyadic Green's functions, will continue to be essential for the insertion of circulators into the next generation of microwave and millimeter wave components.

BIBLIOGRAPHY

1. H. Bosma, On stripline Y-circulation at UHF, *IEEE Trans. Microw. Theory Tech.,* **MTT-12**: 61–74, 1964.
2. R. F. Soohoo, *Theory and Application of Ferrites,* Englewood Cliffs, NJ: Prentice-Hall, 1960.
3. H. S. Newman and C. M. Krowne, Analysis of ferrite circulators by 2-D finite element and recursive Green's function techniques, *IEEE Trans. Microw. Theory Tech.,* **MTT-46**: 167–177, 1998.
4. C. M. Krowne, 2D dyadic Green's function for homogeneous ferrite microstrip circulator with soft walls, *22nd Int. Conf. Infrared Millimeter Waves Dig.,* Wintergreen Resort, VA, 1997, pp. 168–169.
5. C. M. Krowne, Homogeneous ferrite microstrip circulator 3D dyadic Green's function with and without perimeter interfacial walls, *22nd Int. Conf. Infrared Millimeter Waves Dig.,* Wintergreen Resort, VA, 1997, pp. 170–171.
6. C. M. Krowne, Theory of the recursive dyadic Green's function for inhomogeneous ferrite canonically shaped microstrip circulators, in Peter W. Hawkes (ed.), *Advances in Imaging and Electron Physics* vol. 98, New York: Academic Press, 1996, pp. 77–321.
7. C. M. Krowne, Inhomogeneous ferrite microstrip circulator 2D dyadic Green's function for penetrable walls, *Int. J. Electron.,* **85** (1): 121–127, 1988.
8. C. M. Krowne, 3D dyadic Green's function for radially inhomogeneous circular ferrite circulator, *IEEE Microw. Theory Technol. Symp. Dig.,* San Francisco, 1996, pp. 121–124.
9. C. M. Krowne, Ferrite microstrip circulator 3D dyadic Green's function with perimeter interfacial walls and internal inhomogeneity, *Microw. Opt. Technol. Lett.,* **15** (4): 235–242, 1997.
10. R. E. Neidert, unpublished manuscript, 1995.
11. R. E. Neidert and P. M. Philips, Losses in Y-junction stripline and microstrip ferrite circulators, *IEEE Trans. Microw. Theory Tech.,* **MTT-41**: 1081–1086, 1993.
12. J. D. Adam et al., Monolithic integration of an X-band circulator with GaAs MMICs, *IEEE Microw. Theory Tech. Symp. Dig.,* 1995, pp. 97–98.
13. C. M. Krowne, CAD using Green's functions and finite elements and comparison to experimental structures for inhomogeneous microstrip circulators, in P. W. Hawkes (ed.), *Advances in Imaging and Electron Physics,* vol. 106, New York: Academic Press, 1998.

14. C. M. Krowne and R. E. Neidert, Inhomogeneous ferrite microstrip circulator: Theory and numerical calculations using a recursive Green's function, *25th Eur. Microw. Conf. Dig.,* Bologna, Italy, 1995, pp. 414–420.
15. C. M. Krowne and R. E. Neidert, Theory and numerical calculations for radially inhomogeneous circular ferrite circulators, *IEEE Trans. Microw. Theory Tech.,* **MTT-44**: 419–431, 1996.
16. C. M. Krowne, Symmetry considerations based upon 2D EH dyadic Green's functions for inhomogeneous microstrip ferrite circulators, *Microw. Opt. Tech. Lett.,* **16**: 176–186, 1997.
17. C. M. Krowne, Implicit 3-D dyadic Green's function using self-adjoint operators for inhomogeneous planar ferrite circulator with vertically layered external material employing mode-matching, *IEEE Trans. Microw. Theory Tech.,* **MTT-44**: 359–377, 1998.
18. C. M. Krowne, Dyadic Green's function circulator theory for inhomogeneous ferrite with and without penetrable walls, in P. W. Hawkes (ed.), *Advances in Imaging and Electron Physics* vol. 103, New York: Academic Press, 1998.
19. C. M. Krowne, 2D cross-coupling recursive dyadic Green's function, circuit parameters and fields for radially inhomogeneous microstrip circular ferrite circulators, *Microw. Opt. Tech. Lett.,* **17** (3): 140–148, 1998.
20. D. C. Webb, Design and fabrication of low-cost ferrite circulators, *25th Eur. Microw. Conf. Dig.,* Bologna, Italy, 1995, pp. 1191–1200.
21. H. S. Newman, D. C. Webb, and C. M. Krowne, Design and realization of millimeter-wave microstrip circulators, *Proc. Int. Conf. Millimeter Submillimeter Waves Appl. III,* SPIE, Denver, 1996, pp. 181–191.

CLIFFORD M. KROWNE
Naval Research Laboratory

NUMERICAL MODELING OF THE ENVIRONMENT. See ENVIRONMENTAL SCIENCE COMPUTING.
NUSSBAUM FUNCTION. See SWITCHING FUNCTIONS.